6-30-2007

AFCI Quarterly Input – UNLV April 1 through June 30, 2007

Harry Reid Center for Environmental Studies. Nuclear Science and Technology Division

DOE Contract DE-FC07-06ID14781

AFCI Quarterly Input – UNLV
April 1 through June 30, 2007

1.0 University of Nevada, Las Vegas (UNLV)

UNLV Transmutation Research Program. The University of Nevada, Las Vegas supports the AFCI through research and development of technologies for economic and environmentally sound refinement of spent nuclear fuel. The UNLV program has four components: infrastructure, international collaboration, student-based research, and management and program support. Management and program support highlights are the following:

- Administrative and financial management of the UNLV Transmutation Research Program.
- A GNEP poster was prepared and displayed at the Las Vegas Grand Prix April 6-8 and Pahrump Earth Day Festival on April 21.
- A tour of the Nevada Test Site was organized for the UNLV community. Two bus loads of mainly students and staff participated in the tour on April 12.
- Jill Duggan and Annabelle Malins from the United Kingdom embassy gave presentations entitled "The Energy Challenge – Moving to a Low Carbon Future: The UK experience in developing climate policy." Meetings with UNLV faculty occurred in which nuclear power was promoted as part of the solution on April 16.
- Tom Ward, GNEP liaison and TRP science adviser visited UNLV to discuss infrastructure and potential future aspects of the UNLV program April 23-26.
- UNLV hosted the GNEP Economic Analysis Working Group meeting May 1 and 2.
- UNLV was represented at the NEDHO Visit to Congress meeting in Washington, DC. May 3 and 4.
- Three UNLV faculty members attended the AFC Workshop hosted by Boise State University May 8 and 9.
- A GNEP poster was prepared and displayed at the Las Vegas Family and Kids Expo in Las Vegas May 26 and 27.
- UNLV submitted 12 NERI-C proposals (7 as the lead university).
- UNLV hosted the GNEP Safeguards Working Group meeting June 18 to 20.

1.1 Infrastructure Augmentation

1.1.1 Infrastructure Augmentation Scope

The infrastructure augmentation component of the UNLV Transmutation Research Program enhances UNLV's research staff, facilities, and academic programs to increase the ability of the university to perform AFCI research.

1.1.2 Infrastructure Augmentation Highlights

- Dr. Tyler Sullens was hired as a new Assistant Research Professor at the Harry Reid Center for Environmental Studies to support the UNLV radiochemistry academic and research programs.

- Architectural drawings for three new radiochemistry and nuclear engineering laboratories were completed. Remodel for these laboratories is expected to be completed by Spring term 2008.

1.2 International Collaboration

1.2.1 International Collaboration Scope

The international collaboration component of the UNLV Transmutation Research Program enhances UNLV's breadth of scientific and scholastic experience. University collaboration is also an efficient conduit for international collaboration that benefits the national AFCI program. UNLV has ongoing relationships with the International Science and Technology Center (ISTC) and the Khlopin Radium Institute (KRI) in St. Petersburg, Russia.

1.2.2 International Collaboration Highlights

The contract with the Khlopin Radium Institute to perform an upgrade to the UNLV Neutron Multiplicity Detector System is still in negotiation. The challenging issue has been the duration of the scope of work which goes beyond the current UNLV contract extension date with DOE of August 31, 2007. The UNLV administration is hopeful that assurances of the intent to extend beyond this contract end date will be sufficient to complete the new UNLV/KRI contract.

1.3 Student Research

1.3.1 Student Research Scope

The Student Research component is the core of the UNLV Transmutation Research Program. The milestones, schedules, and deliverables of the student research projects are detailed in the individual research proposals. UNLV has 21 active student research tasks and 15 tasks that have concluded. The tasks are divided below in terms of the following research areas: fuels, separations, and transmutation sciences.

1.3.2 Student Research Highlights

FUELS TECHNOLOGY

Interaction between Metal Fission Products and TRISO Coating Materials (Task 17) Highlights.

- SiC wafer was received from vendor. Pristine SiC surface was characterized and sample cleaning was prepared.
- Analysis continued of data obtained on the Cs/SiC samples that were investigated with Photoemission and Scanning Probe Microscopy at UNLV and with X-ray Emission Spectroscopy during the March experimental run at the Advanced Light Source, Lawrence Berkeley National Laboratory.
- Significant time was devoted to the maintenance of the Ultra High Vacuum system. In particular, the base pressured was lowered by more than one order of magnitude through optimized baking and Ti sublimation pump utilization. This is of crucial importance for the experimental campaign on the interface formation between Cs and very clean SiC or highly

ordered pyrolytic graphite (HOPG).

- Experiments for Cs on HOPG were prepared and Cs was stepwise deposited on HOPG. Samples were investigated by X-ray and UV-photoelectron spectroscopy as well as atomic force microscopy.
- The Pd evaporator needed for the Pd/SiC experiments was mounted on the chamber, degassed, and baked.

Dissolution, Reactor, and Environmental Behavior of ZrO_2-MgO Inert Fuel Matrix (Task 19) Highlights.

- The Soxhlet concluded with three new samples: $Zr_{0.885}Mg_{0.05}U_{0.05}Er_{0.025}O_{1.96}$, $Zr_{0.725}Mg_{0.2}U_{0.05}Er_{0.025}O_{1.79}$, and $Mg_{0.925}U_{0.05}Er_{0.025}O_{1.06}$.
- Another crushed pellet with lower Mg content contacted with HNO_3 and no U leaching was observed; dissolution studies continued.
- UY_6O_{12} was synthesized for the Los Alamos National Laboratory group. Delta phase was confirmed by XRD. The pellets were repressed and sintered to obtain good quality pellets.
- Dissolution data analysis for University of Florida was finalized. The process for obtaining Pu containing inert matrix fuels from INL was begun.

Design Concepts and Process Analysis for Transmuter Fuel Manufacturing (Task 22) Highlights.

- Mathematical concepts and code were developed and tested for the spatial analysis of Stereo images and for stereo vision system calibration.
- Two-camera stereo vision system was set up in the lab, calibrated and tested. Multiple experiments were conducted and the accuracy of the calibration was measured. The accuracy of the position detection algorithm was verified experimentally. Corrections to improve geometrical accuracy were made and tested.
- A robot gripper for fuel pellet grasping was designed and ordered.

Impact of the Synthesis Process on Structure Properties for AFCI Fuel Candidates (Task 28) Highlights.

- Chemical phase identification was performed using X-ray powder diffraction (XRD) while these XRD patterns were further used to quantify the phase distributions of the samples using Rietveld analysis. The lattice parameter of each phase was also refined using Rietveld refinement.
- Rate constants (k) of UN_2 reduction to UN under argon were determined at 1000, 1050, and 1100 C temperatures.

Solution-based Synthesis of Nitride Fuels (Task 34) Highlights.

- A procedure to clean the oxide coating from uranium metal was developed and tested under synthetic conditions to ensure the viability of maintaining a clean metal surface while submerged in liquid ammonia.
- Several reactions were carried out in an attempt to synthesize the $UI_3(NH_3)_x$ precursor to the UN final product under the conditions specified in the proposal.

SEPARATIONS TECHNOLOGY

Immobilization of Fission Iodine (Task 15) Highlights.

- Synthetic approaches continued to be explored to produce MnO_2 that would be suitable for the oxidation of iodide.
- The dissolution behavior of various MnO_2 samples was examined in the presence of citric acid and pyrophosphate.
- Surface charge and the pH of zero charge were determined for various samples.
- TEM and scanning electron microscopy was used to characterize the surface morphology of various samples.

Development of Integrated Process Simulation System Model for Spent Fuel Treatment Facility Design (Task 24) Highlights.

- The addition of the CCD_PEG module implementation based on the Argonne National Laboratory (ANL) request was completed.
- The second program revision based on the internal testing results was completed.
- The first draft of the ISOPro User Manual under the second revision was completed.

Electrochemical Separation of Curium and Americium (Task 25) Highlights.

- The electrochemical response of Eu in room temperature ion liquids (RTIL) was evaluated.
- Immidazolium cations were prepared for the next series of RTIL solutions.
- The electrochemistry of Uranium species in RTIL solutions was examined.

Fundamental Chemistry of U and Pu in the TBP-Dodecane-Nitric Acid System (Task 26) Highlights.

- Uranium extraction studies: organic phase of samples prepared by an organic phase and an aqueous phase were titrated, samples for more inductively coupled plasma atomic emission spectroscopy (ICP-AES) and liquid scintillation counter comparisons were prepared, and research and preliminary experiments began on the determination of uranyl nitrate stability constants.
- Acetohydroxamic acid (AHA) studies: evaluation of Uranium AHA crystals continued, AHA coordination was examined by NMR, the presence of U was examined for affect on reduction rate of Tc and extraction of Tc in presence of AHA, the kinetics were measured in multicell changer for 5 hours, and the extraction of Tc and U with TBP in the presence of AHA was examined.
- Studies were performed on Specific Ionization Theory/Effect of ionic strength on AHA pKa.

Investigation of Optical Spectroscopy Techniques for On-Line Materials Accountability in the Solvent Extraction Process (Task 29) Highlights.

- Investigation were initiated into impact of iron on detection limits of uranium in raffinate streams.

Combined Radiation Detection Methods for Assay of Higher Actinides in Separation Processes (Task 30) Highlights.

- Modeling of the Neutron Multiplicity Detector System (NMDS) was expanded and improved, and K and t-zero values (energy-time correlation constants) were benchmarked against a LANL experiment and model.
- Installation of coaxial cables in the new digital data acquisition system of the Neutron Multiplicity Detector System (NMDS) reduced background count rates (noise).
- Several new collaborations were initiated with the V. G. Khlopin Radium Institute, Idaho National Laboratory, Los Alamos National Laboratory, Renssellaer Polytechnic Institute, and Idaho State University.

Synthesis and Properties of Metallic Tc and Tc-Zr Alloys as a Radioactive Storage Waste Form to Stabilize the Tc Waste Stream of the UREX+1 Process (Task 33) Highlights.

- Static experiments were carried out in the aims of determining Tc absorption capacity and elution properties of treated resins.
- Dynamics experiments were performed on simulated UREX solution in order to determine the separation factor U/Tc and to study the possibility of a Tc elution from the resin.

Evaluation of Cs/Sr Waste Form for Long Term Storage and Disposal (Task 36) Highlights.

- The project kick-off meeting with DOE collaborators took place.
- Sample matrix was developed for materials interactions testing.

TRANSMUTATION SCIENCES

Corrosion Mechanisms and Kinetics of Steels in Lead-Bismuth Eutectic (Task 18) Highlights.

- Peak fitting of Raman data was demonstrated – 3 cm^{-1} resolution was seen.
- Furnace section of the liquid metal corrosion test facility was tested.
- Gas phase modeling experiments were conducted and XPS data was collected.
- D9 samples from LANL were investigated exhaustively by SEM and Atom Probe.

Impact of Silicon on Corrosion Resistance of Stainless Steels in LBE Systems (Task 20) Highlights.

- The results of tensile testing involving activated smooth cylindrical specimens of all four heats have been obtained and viewed in the form of superimposed engineering stress versus strain (s-e) diagrams.
- The magnitudes of both initial stress intensity factor (K_i) and final stress intensity factor (K_f) were obtained from double cantilever beam testing.
- An evaluation of the C-ring and U-bend specimens by SEM revealed intergranular cracking on the convex surfaces of a few specimens.

- Immersion testing was conducted involving coupons of four heats of T91 grade steel in a 100 C acidic solution.
- The tensile testing involving smooth cylindrical specimens of martensitic steels containing higher Si content (2.75, 4.83 and 5.27 wt%) were conducted at different temperatures.

Oxide Film Growth Modeling in LBE Systems (Task 21) Highlights.

- A parametric study on the mesoscopic oxidation model with the cellular automaton (CA) method on the oxidation process coupled with inward oxygen diffusion was completed.
- An intensive literature survey was conducted on the corrosion and erosion modeling using molecular dynamics (MD) techniques, in particular, on the simple binary systems using Moldy, which is a free and open source code.

Corrosion Barrier Development for LBE Corrosion Resistance (Task 23) Highlights.

- Templates were created for the fabrication of nanowires using the technique of nanoparticle incorporation.
- Cr nanoparticle synthesis was initiated to be used for the formation of the nanowires.
- Preliminary temperature cycling was carried out on previous samples that will be sent to a vendor for surface adhesion characterization.
- The development of process technology for the fabrication of nanowires through the incorporation of nanoparticles was completed.

Reactor Physics Studies for the AFCI RACE Project (Reactor-Accelerator Coupling Experiments Project (Task 27) Highlights.

- Evaluation continued of ISU experiments conducted in collaboration with CEA (France) during the RACE-ECATS phase of the project.
- Evaluation continued of experimental thermal and neutron generation with the UNLV High-power RACE target (experiments were conducted at ISU).

Decoupling and Disturbance Rejection Control for Target Circulation (Task 31) Highlights.

- The whole Target Complex 1 (TC-1) system was tested and continuously operated for 20 days.
- Several problems were found and options for solving the problems were made.

Magnetohydrodynamic Simulation of Electromagnetic Pump in TC-1 (Task 32) Highlights.

- An online database of articles and papers related to EM pump technology was created. This database is currently being expanded and reorganized using wiki-based software to allow greater interaction and information sharing between the project researchers.
- A fully coupled magnetohydrodynamic (MHD) solver, working title EMPUMPER, is nearing completion. This application has been developed in-house using Fortran 90 and thus will be cross-platform capable.

Criticality Studies for UREX Processes (Task 35) Hightlights.

- The NJOY99 cross section processing code was acquired and installed for use with other code systems in sensitivity studies.

1.3.3 Student Research Technical Reports

FUELS TECHNOLOGY

Interaction between Metal Fission Products and TRISO Coating Materials (Task 17).

The experimental focus this quarter was on the investigation of the Cs/HOPG interface. For this purpose, a series with Cs films of different thickness on HOPG were prepared. UV photoemission (UPS), x-ray photoemission (XPS), and in-vacuum atomic force microscopy (AFM) experiments were performed for each Cs film thickness. HOPG substrates were prepared by cleaving under nitrogen in the glove box directly connected to the surface analysis system at UNLV and then directly introduced into the UHV apparatus without any air exposure.

The XPS survey spectra for different Cs evaporation times (and hence different Cs film thicknesses) are shown in Figure 1. The cleaving of the sample under nitrogen clearly results in a very clean and nearly adsorbate-free surface, as can be seen from the weak O 1s line in the bottom-most spectrum (figure 1). After Cs evaporation, all expected Cs lines can be found in the spectra. The intensity of the lines, which can be related to the film thickness, increases for increasing deposition time, as expected. In parallel, the lines of the HOPG substrate (i.e., the C 1s photoemission line and the C KVV Auger line) decrease in intensity due to the attenuation by the covering Cs layer.

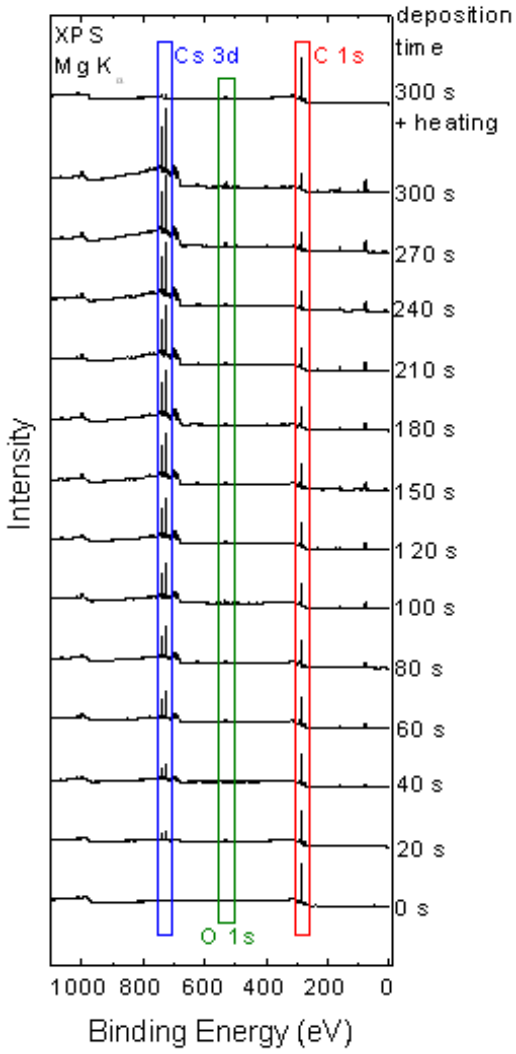

Figure 1: XPS survey spectra of an HOPG substrate, as well as after stepwise deposition of Cs and subsequent heating under inert conditions.

Currently, a quantitative analysis of the individual XPS peaks (detailed spectra are not shown) is in progress. Nevertheless, judging from the survey spectra, first trends can already be derived. The Cs 3d intensity shows a fast increase for short deposition times, and only a weak increase after about 30s of deposition time. In contrast, the C lines are only weakly attenuated, suggesting that the formed film of Cs does not exhibit a uniform thickness, but rather that an island-like growth is taking place.

This interpretation is corroborated by the AFM images recorded after subsequent deposition steps. A compilation of some of these images is shown in Figure 2. The image of the pure HOPG surface before Cs deposition (Figure 2a) shows a clean surface with a number of mono-atomic steps. After the first few deposition steps, small Cs islands formed on the HOPG surface, as shown in Figure 2b. After additional deposition steps, the Cs islands increase in number. The image in Figure 2c also shows that they preferably grow along the mono-atomic steps of the HOPG substrate.

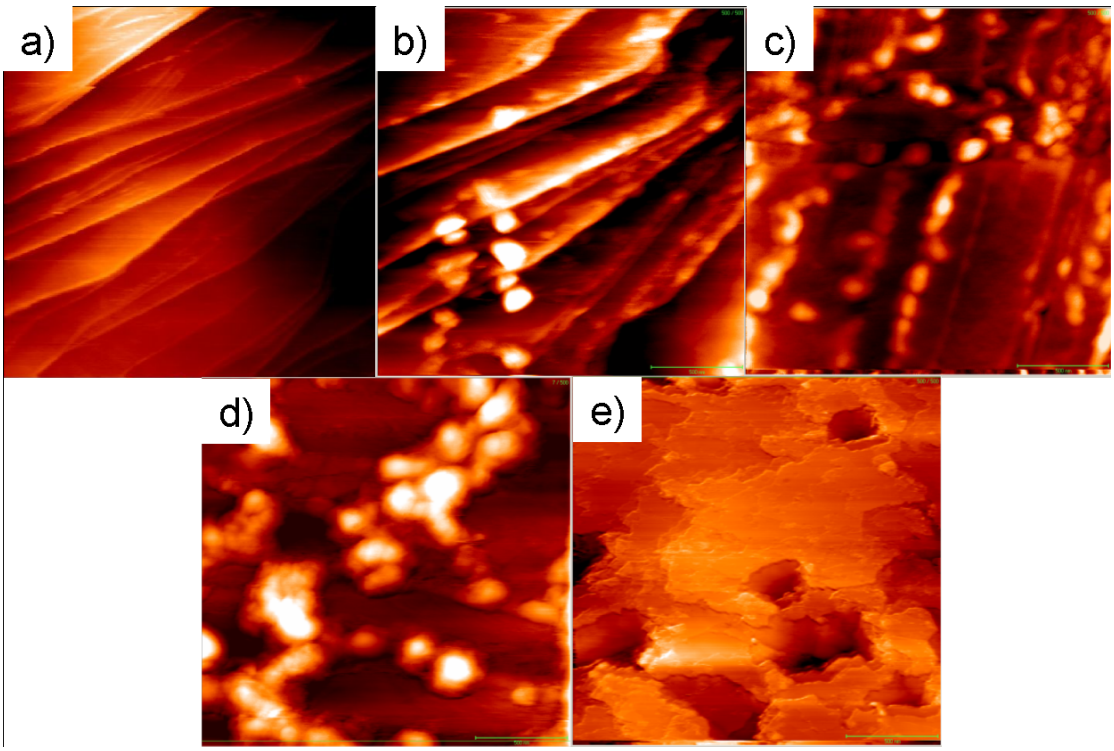

Figure 2: Atomic Force Microscopy (AFM) images of (a) HOPG, after (b) 40 sec, (c) 120 sec, (d) 300 sec of Cs evaporation, and after (e) 300 sec of Cs evaporation and subsequent heating to 600°C for one hour under inert nitrogen conditions. The size of all images is 2µm x 2µm, and all samples were prepared and studied in an ultra-high vacuum.

No further increase in the density of islands, but rather a strong three-dimensional growth of the already existing islands, is observed after the next deposition steps (Figure 2d).

To simulate the high-temperature environment that the TRISO particles have to sustain in operation, the thickest of the deposited Cs films has been heated ex-situ under inert conditions in a furnace. The sample was heated for one hour at 600 C (purposely held about 70 C below the boiling point of Cs).

The XPS survey spectrum (top-most spectrum in Figure 1) reveals a strong decrease in Cs intensity, which can be interpreted as a loss of Cs from the surface due to evaporation or a diffusion of Cs into the HOPG film. After heating, strong changes in the surface morphology can be found, as seen in the AFM image in Figure 2e.

As a next step, and complementing the measurements of Cs/oxidized SiC, the focus will be on the investigation of the Cs/single crystalline SiC interface inspecting the role of SiC as diffusion barrier for Cs.

Dissolution, Reactor, and Environmental Behavior of ZrO_2-MgO Inert Fuel Matrix (Task 19).

The soxhlet study has concluded for uranium containing ceramics. A total of six samples have been analyzed, ranging from an inert matrix of completely ZrO_2 to completely MgO with four samples of

mixed phases. They have shown that ZrO_2 enhances corrosion resistance as illustrated in Figures 3 to 5.

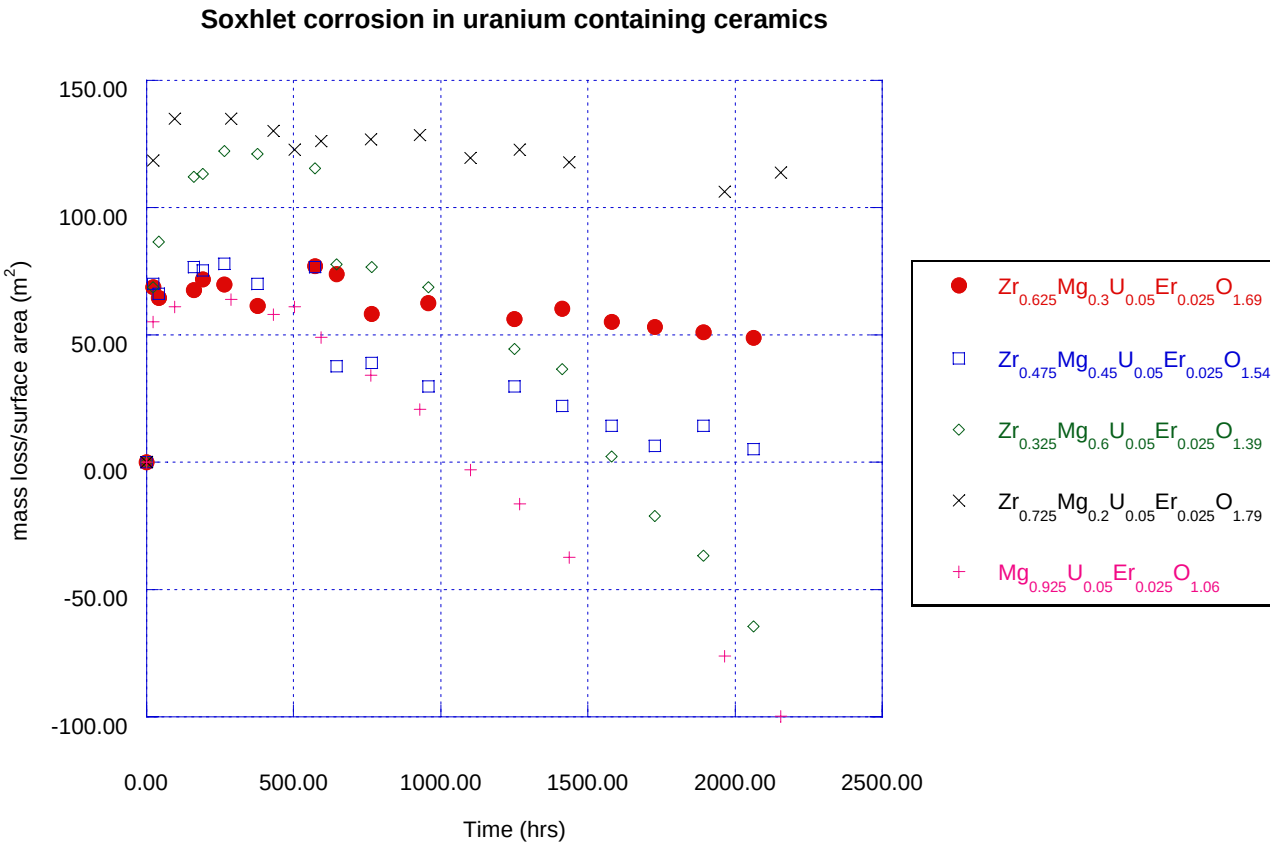

Figure 3: Soxhlet corrosion in uranium-containing ceramics.

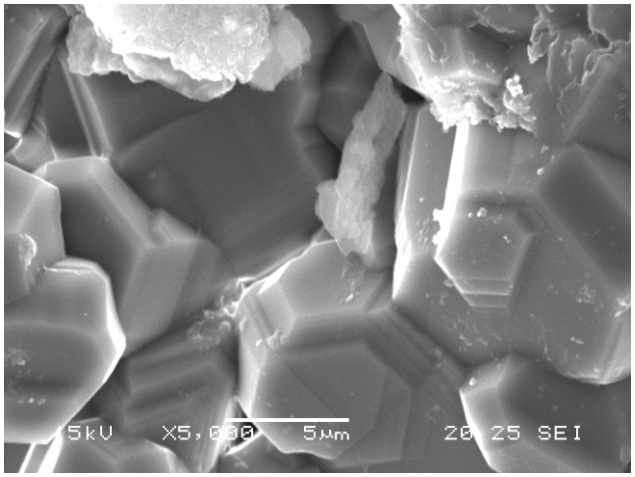

Figure 4: High zirconium content shows little signs of corrosion even under high magnification (5,000x).

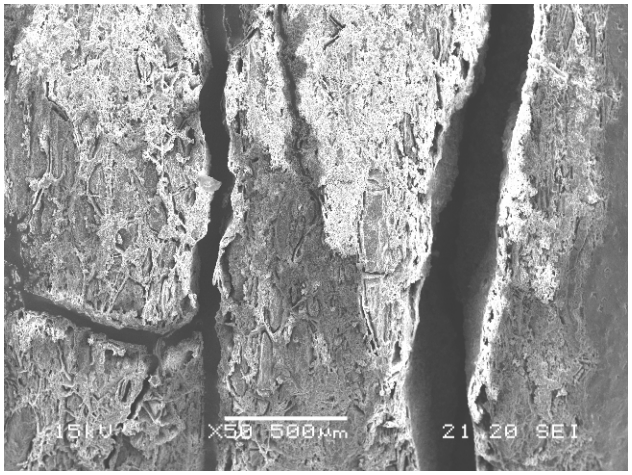

Figure 5: High magnesium content show detrimental corrosion damage even at low magnification (50x).

Dissolution studies with nitric acid have shown a linear dissolution rate for uranium; however improvements are needed for consistent kinetic constants. Also uranium leaching in nitric acid is only possible at high magnesium concentrations. This is because of the greater surface area of

the exposed zirconia phase once the magnesia is dissolved, and the higher uranium concentration within the zirconia phase in these samples. Dissolution in supercritical water was extended to 3 weeks with the same results. Only magnesium is found in solution.

UY_6O_{12} pellets were synthesized for Los Alamos National Laboratory for initial waste form studies complementary to the inert fuel research. Composition was confirmed to be delta phase by X-ray diffraction.

Two pellets received from the University of Florida (60/40 vol. % MgO-$Zr_2Nd_2O_7$) were exposed to near boiling H_2SO_4 for one week. Mg and Nd were well described by first order dissolution kinetics (see Figures 6 and 7). Equilibrium concentrations were accurately established, however further experiments are needed to better describe the dissolution constant (k). Zr was suspended in solution, but is not soluble and therefore poorly described by the dissolution equation. It is however quite possible to dissolve the settled Zr material in HNO_3 after treatment with H_2SO_4.

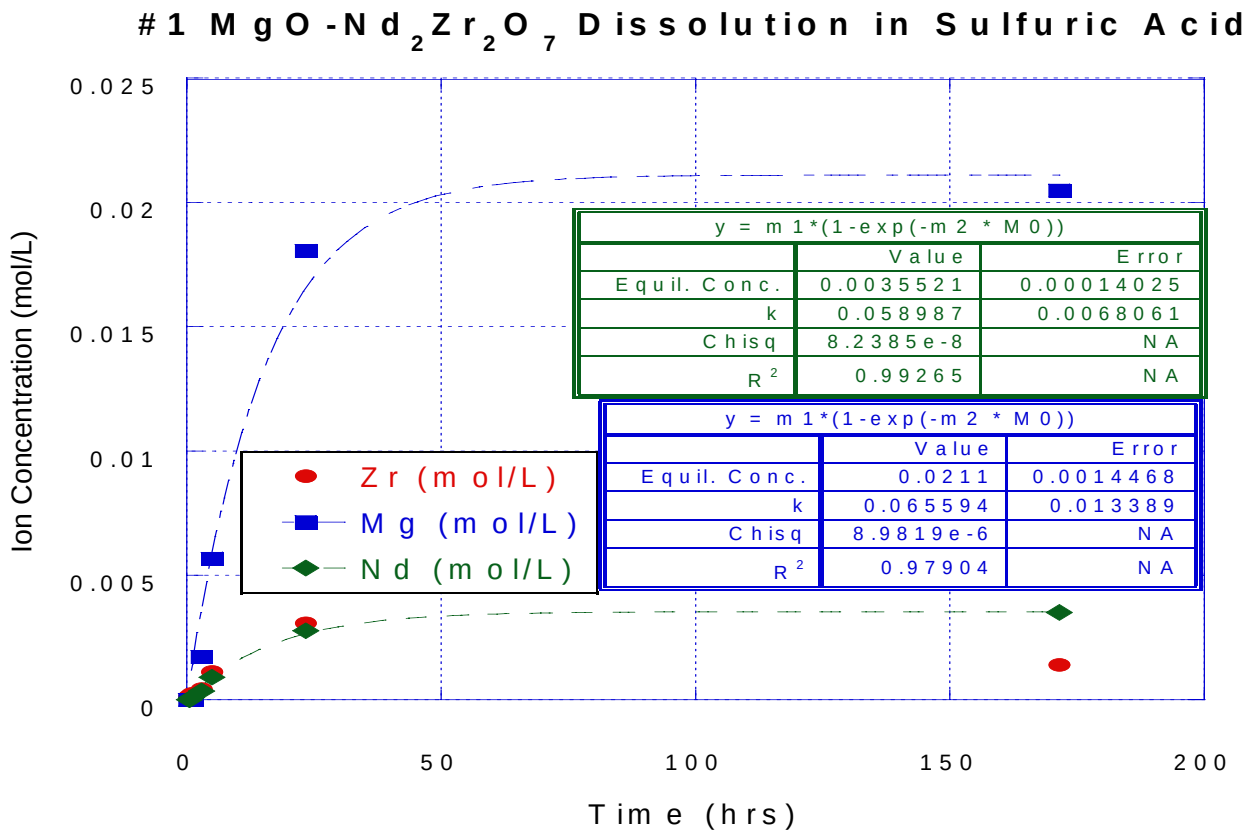

Figure 6: MgO-$Nd_2Zr_2O_7$ dissolution results in sulfuric acid (Pellet 1).

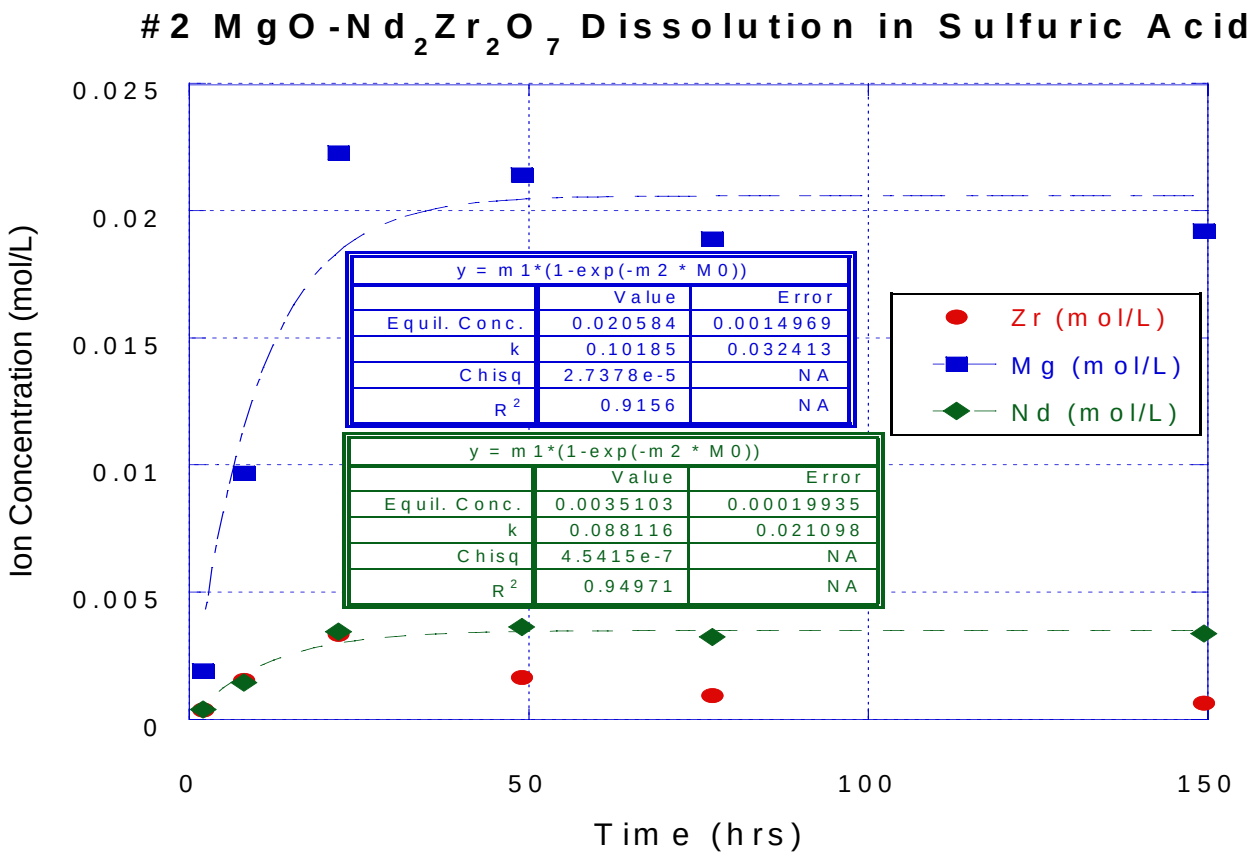

Figure 7: $MgO\text{-}Nd_2Zr_2O_7$ dissolution results in sulfuric acid (Pellet 2).

Design Concepts and Process Analysis for Transmuter Fuel Manufacturing (Task 22).

Hot Cell robot control

Work continued on the visual servoing of robots inside the hot cell. Camera calibration (Figure 8) and spatial range measurements from two spatial locations (stereo vision) continued to be a focus.

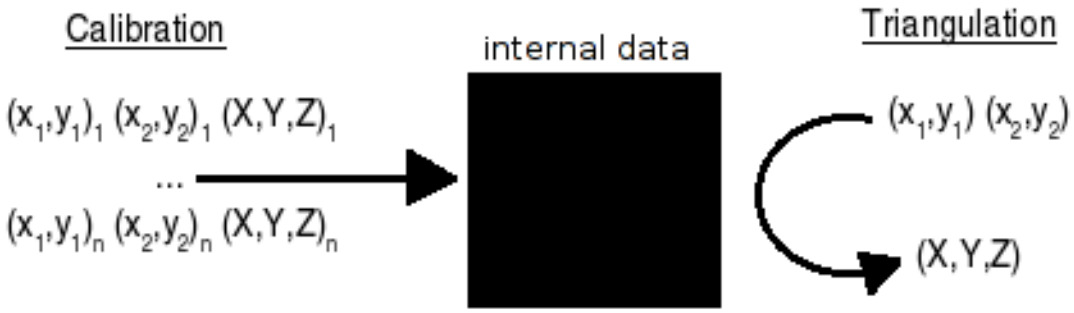

Figure 8: Camera calibration concept.

Determination of Object Location and Orientation

The location and orientation of fuel pellets were found by measuring their contour and top and bottom surface centers (Figure 9).

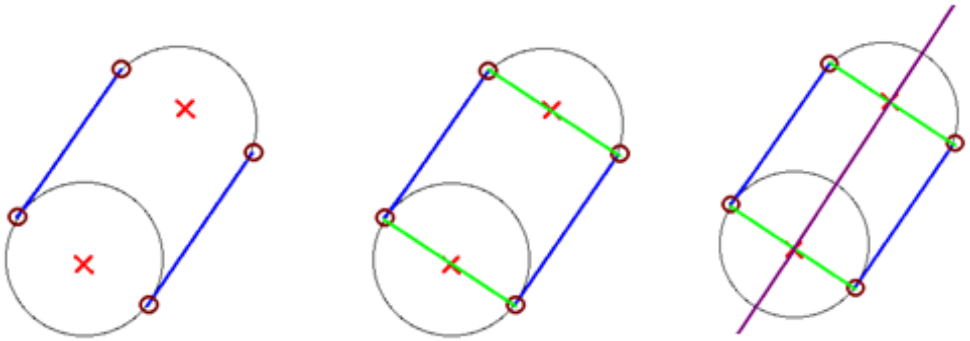

Figure 9: Finding an object's spatial orientation.

Image Noise reduction

Since the image consists of discrete pixels, interpolation along lines can reduce uncertainty and increase accuracy. A noise reduction algorithm was implemented and tested.

Automatic Calibration of a Test Scene

A black conical tip was built and attached to an industrial robot. This approach has the advantage that the calibration can be easily done in the robot's own coordinate system (Figure 10). The application for the calibration is written in Visual Basic connected to a Matlab interface. Since both languages are needed (Visual Basic to control the robot, Matlab to proceed the image processing), both programs were merged. For the calibration, the robot end effector is steered to a desired position visible in both camera images. Then a Matlab function is called to capture the images and extract the top of the tip as a reference point. This procedure is repeated for several coordinate locations within the scene.

Figure 10: Industrial robot with calibration tip.

The length of the tool tip used in this application is much larger than its diameter. This makes the triangle found in the images unique.

To extract the triangular shape formed by the black tip from the image, the following algorithm is used:

- Improve image brightness and contrast
- Proceed Canny Edge Detection
- Select a curve that is circular (closed, end point = start point)
- Extract the curve as a chain code sequence
- Extract corners and calculate the straight line representation of the two longest edges
- Check the lines: if the angle between these lines or the distance of the real curve and the straight lines possess deviations, select another closed curve and proceed the accordant steps
- Calculate intersection of the two straight lines (top of the sting)

The automatic calibration algorithm has been tested and is operational on the industrial robot.

Impact of the Synthesis Process on Structure Properties for AFCI Fuel Candidates (Task 28).

Characterization Methods

Chemical phase identification was performed using X-ray powder diffraction (XRD) while these XRD patterns were further used to quantify the phase distributions of the samples using Rietveld analysis. The lattice parameter of each phase was also refined using Rietveld refinement.

Reaction kinetics of UN formation from UN_2

Rate constants (k) of UN_2 reduction to UN under argon were determined at 1000, 1050, and 1100 C temperatures, and are shown in Figure 11 through Figure 13, respectively. The activation energy of the reaction calculated using the Arrhenius plot (Figure 14) using these k-values is 423.8 kJ/mol.

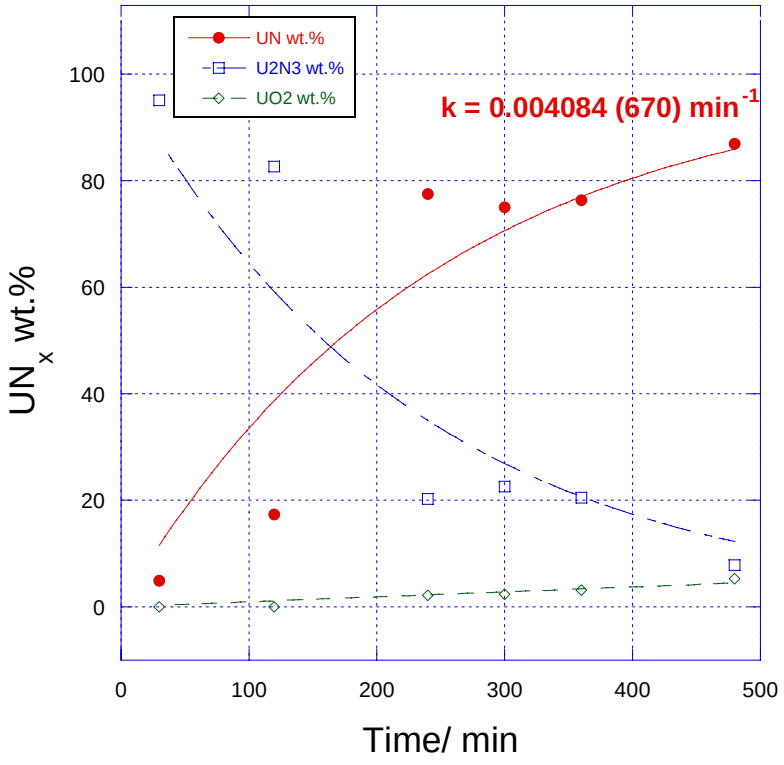

Figure 11: Pseudo-first-order kinetics of UN_2 denitriding at 1000 C.

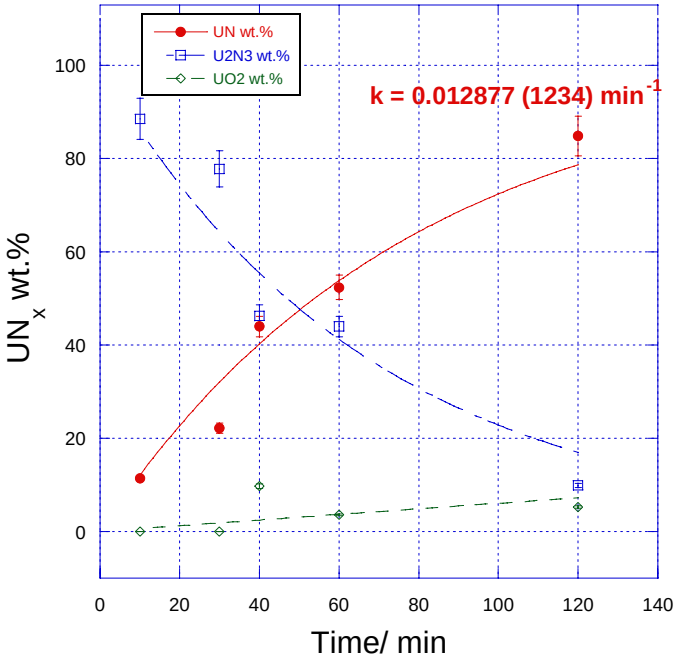

Figure 12: Pseudo-first-order kinetics of UN_2 denitriding at 1050 C.

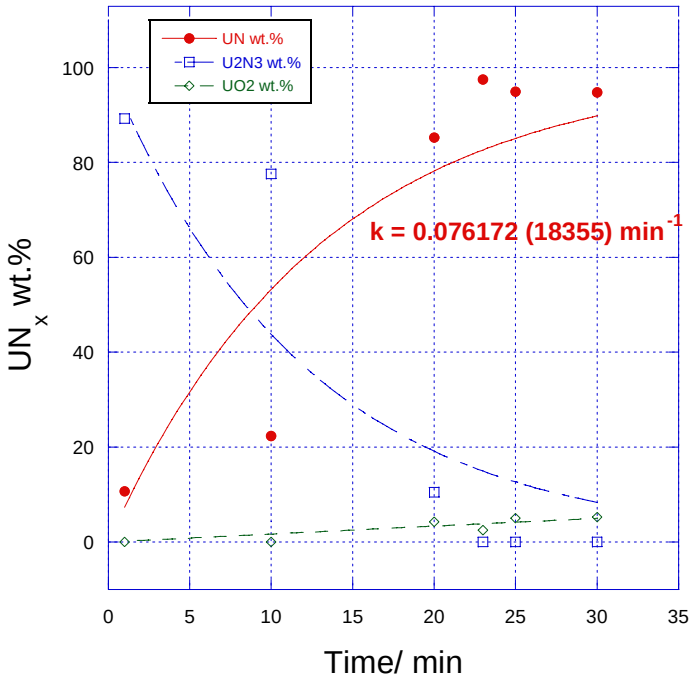

Figure 13: Pseudo-first-order kinetics of UN_2 denitriding at 1100 C.

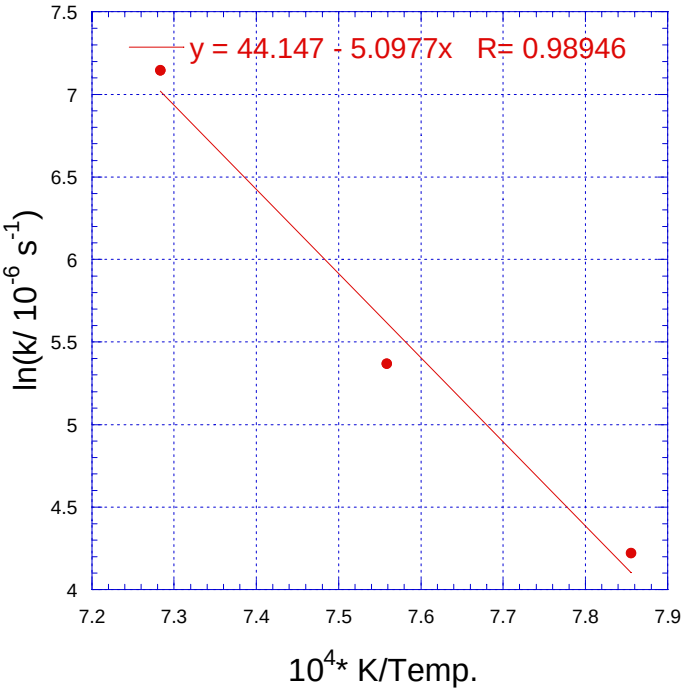

Figure 14: Arrhenius plot for the UN_2 to UN reaction.

The lattice parameter of the UN_2 samples heated at different temperatures showed a linear variation with respect to the temperature (Figure 15). Furthermore, it was seen that the lattice parameter increases as the temperature increases. Increase in the UN_2 lattice parameter also

happens when the N:U molar ratio decreases (Tagawa, 1974). This observation confirms that UN_2 approaches the UN_2-U_2N_3 phase boundary as the temperature increases.

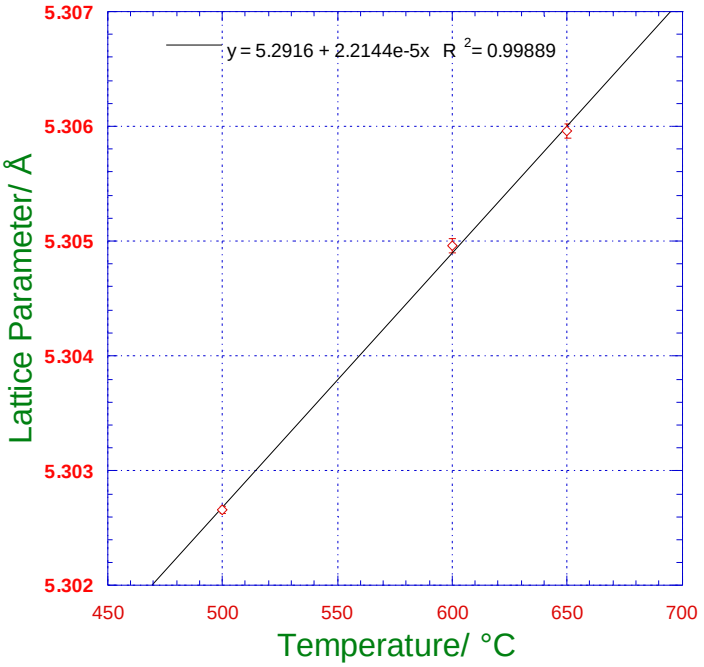

Figure 15: Lattice parameter of UN_2 as a function of temperature.

A similar observation could be seen for the U_2N_3 samples synthesized at different temperatures starting from 700 C (Figure 16). That is, the U_2N_3-UN phase boundary is reached by U_2N_3 when it is heated up to 1000 C. Furthermore, a plot of N/U EDX peak intensity ratios obtained from TEM-EDX of U_2N_3 as a function of temperature (Figure 17) verifies the fact that the nitrogen removal continued and is increased as the temperature used to synthesize the samples increases. Thus the UN_2 denitriding under argon atmosphere involves through U_2N_3 intermediate phase which could be formed after 675 C. The U_2N_3 decomposition to UN happens at temperatures after 975 C.

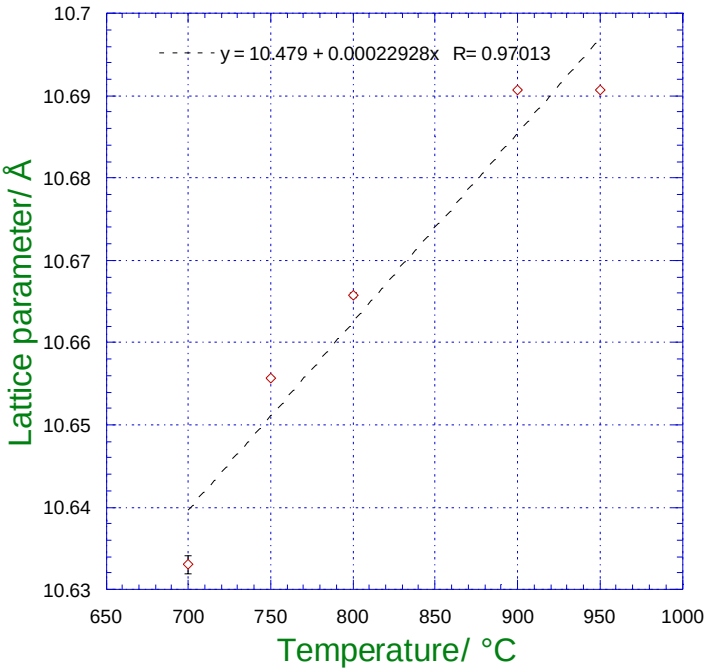

Figure 16: Lattice parameter of U_2N_3 as a function of temperatures.

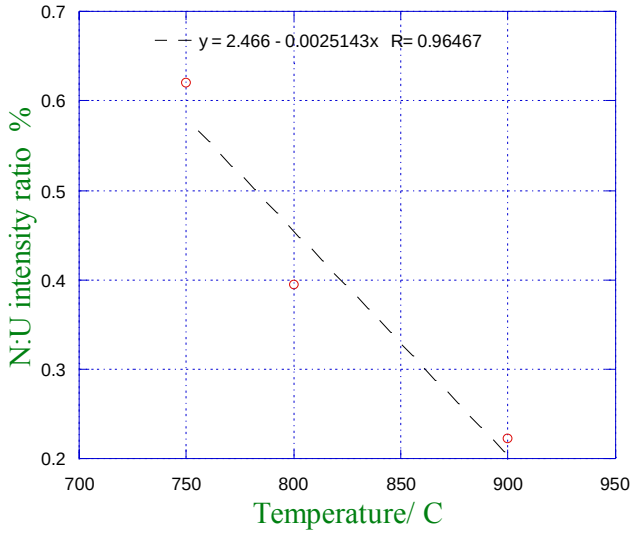

Figure 17: N/U EDX peak intensity ratio of U_2N_3 as a function of temperature.

Solution-based Synthesis of Nitride Fuels (Task 34).

Maintaining the trivalent oxidation state of uranium in the intermediate products ($UI_3(NH_3)_x$ and $U(NH_2)_3(NH_3)_x$) in this synthetic scheme is difficult due to the high probability of water and oxygen contamination in ammonia. Air and water sensitive syntheses are normally carried out in organic solvents that can be purified through distillation along with sorption or chemical reactions. Due to the low boiling point of ammonia, this project is limited by the purity of ammonia available from industrial sources. Literature reviews have been conducted to develop a

procedure to dry and deoxygenate the ammonia solvent prior to use in the reaction, but the information for this process is limited. Other adaptations from literature are also tedious due to the disparities between using liquid ammonia as an air sensitive solvent and using common organic solvents. However, one of the significant synthetic obstacles surmounted is the removal of oxide coating from the uranium metal. This was accomplished by several washings of the metal turnings with concentrated nitric acid, each followed by a thorough washing with liquid ammonia. The removal of the oxide coating results in a noticeably lustrous metal remaining that can be stored for a practical amount of time either under liquid ammonia or under argon atmosphere. This process is highly exothermic and results in ammonium nitrate and uranyl nitrate as byproducts.

Reactions performed with a clean uranium surface have given indications that this reaction scheme can be performed as planned. Several parameters have been adjusted, as anticipated, and will continue to be modified in order to synthesize the desired product and obtain the highest yield. One of the main considerations thus far is the reaction time necessary to produce the $UI_3(NH_3)_x$ intermediate. The rapid boiling of the ammonia solvent prevents the reaction from being maintained under ideal conditions for an extended period. Therefore, regular additions of solvent are required so that the reaction may proceed to completion. With impure solvents, these regular additions increase the likelihood of contamination and oxidation of uranium to the tetravalent state, thus rendering the reaction useless. Every possible measure will be taken in order to maintain reaction purity under the proposed synthetic regime. However, contingency plans are being prepared in order to prepare the appropriate precursors for UN by literature methods, should the high purity of ammonia not be available.

SEPARATIONS TECHNOLOGY

Immobilization of Fission Iodine (Task 15).

Various synthetic methods were examined to determine how reaction conditions can influence the MnO_2 product (phase, particle size) produced by the reaction of $KMnO_4$ with various reducing agents. Temperature, reagent concentration, pH and stirring rate have been varied during this study. Stirring rate did not appear to influence product distributions (mineral phase or crystal size). For the product produced by the reaction of $KMnO_4$ with HCl, it was found that temperature had a large influence on reaction kinetics. However, more favorable reaction kinetics could be achieved (at lower HCl concentration and room temperature) by adding NaCl (3M) to the reaction mixture. The products were similar with both procedures. Variation in solution volume (at identical reagent concentrations) had no influence on product distributions, an indication that synthetic methods can be scaled up to produce larger quantities of product.

The dissolution behavior of various MnO_2 products has been examined in the presence of both pyrophosphate and citric acid. These reagents were selected because they have been utilized in previously published studies of MnO_2 reactivity. Pyrophosphate is a chelating agent that is known to form stable complexes with Mn(II) and Mn(III). Citric acid is a chelating agent as well as a reducing agent. All experiments were conducted at pH 4 with ~2mM pyrophosphate or citrate. Dissolution was followed using the UV/Vis spectrophotometer described in previous reports. MnO_2(s) suspensions have a broad absorbance from 250 to 700 nm. 500 nm was

selected as a measure of solid manganese oxide concentrations. An example of the results obtained from this analysis is shown in Figure 18. In this example, ~80 µg of the oxide is suspended in 2 mL of pH 4 acetate buffer. A 50 uL aliquot of pyrophosphate solution (resulting in a concentration of ~2 mM) was added, and the absorbance was monitored as a function of time. As illustrated, absorbance increased with time indicating that light scattering was increasing. Absorbance spectra were periodically recorded and an absorption band increased at ~260 nm indicating the possible formation of a soluble metal complex. The increase in absorbance at 500 nm is ascribed desegregation of the manganese oxide. It is believed that the chelating agent is removing bridging cations (possible Mn^{+2}) from between particle surfaces resulting in desegregation. The addition of citrate (~ 2mM) to the pyrophosphate treated suspension results in a decrease in light absorption, after a brief induction period. This is also illustrated below. It is believed that this resulted from reductive dissolution of the manganese oxide. The UV/VIS spectra obtained have a pronounced absorbance at 240 nm that probably is a result of the formation soluble Mn(II) complexes with pyrophosphate and citrate. In addition, there is another maximum (weak) at 430 nm that the chemical literature indicates corresponds to Mn(III) complexes. Treatment with citrate alone results in an initial increase in light scattering (disagregation) followed by a decrease in light scattering (reductive dissolution). With one sample that was shown to have an average manganese oxidation state close to III, complete dissolution was achieved with pyrophosphate alone. These results corroborate previous studies of manganese oxide dissolution the indicated that Mn(III) is an intermediate in reductive dissolution.

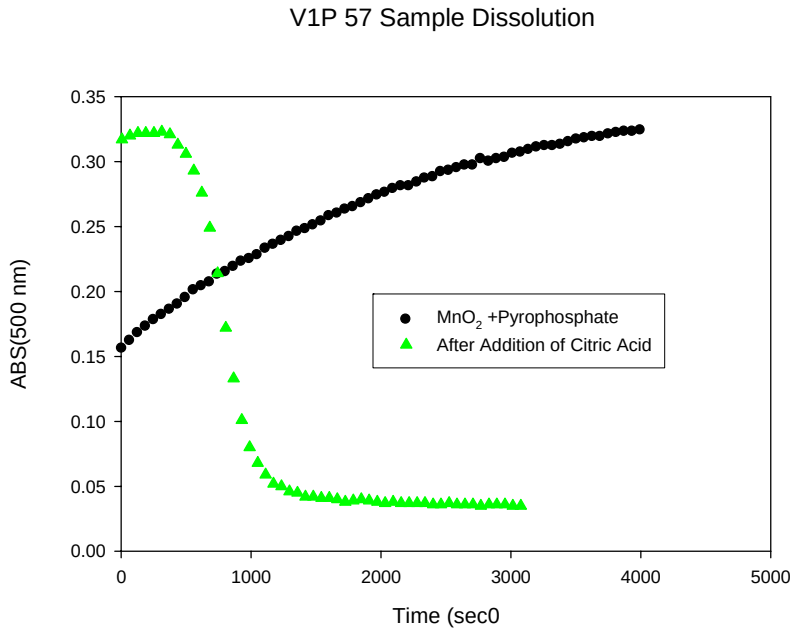

Figure 18: The absorbance at 500 nm was used as a measure of particle concentration. For this sample pyrophosphate increased light scattering while citrate reduced scattering by reductive dissolution.

In order to determine surface charge characteristics of the manganese oxide minerals, titration studies were conducted. Generally 0.5 to 1.0 gram of the sample was suspended in 50.0 mL electrolyte (generally 0.1 M $NaNO_3$) containing 1.0 mL of 0.100 M HNO_3. This mixture was

titrated with 0.1 M NaOH using an automated procedure. Titratant was added in small increments of 0.02 to 0.2 mL so that changes of no more that 8 mV (pH electrode) occurred with each volume addition. The mixture was allowed to equilibrate until the reading was steady (fluctuations or drift less then 0.1 mV/sec). Surface charge was calculated using mass balance. The maximum surface concentration of ionizable functional groups can be estimated using a gran plot method. Two examples of surface charge calculated by mass balance are provided in Figure 19. V4bp10 was prepared with $MnSO_4/MnO_4$ while V1p57 was prepared with HCl/MnO_4. The surface areas are 236 and 22.4 m^2/g respectively. As can been seen in the figure, the pH of zero charge (at 0.1M ionic strength) is ~6.6 and ~3.8 respectively. This illustrates the influence of synthetic methods on surface properties of the mineral product.

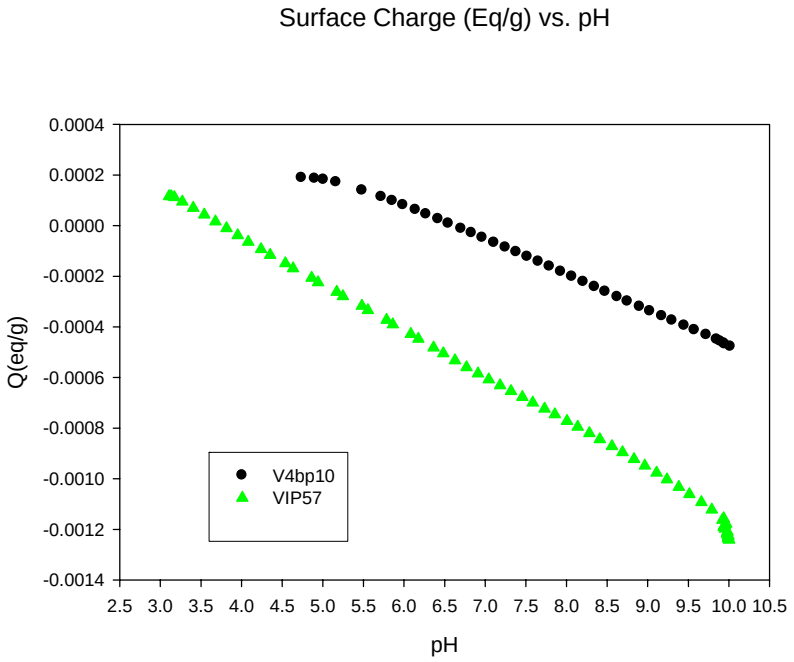

Figure 19: Titration of manganese oxide suspensions with 0.1M NaOH. Using mass balance surface charge (in equivalents/gram) was calculated and the pH of zero charge can be estimated.

TEM and SEM studies were performed for a visual characterization of surface properties. These images indicate that most of the products have amorphous and crystalline regions with variation in morphology that resulted from variations in the synthetic method.

Development of Integrated Process Simulation System Model for Spent Fuel Treatment Facility Design (Task 24).

CCD_PEG module addition

Creation of the CCD_PEG module requires the integration of a new Flow Sheet and Section properties with the main program, ISOPro, as shown in Figure 20. The CCD-PEG module can be enabled or disabled based on the user's need. The completed module has been recompiled with the ISOPro program to generate an up-to-date executable file.

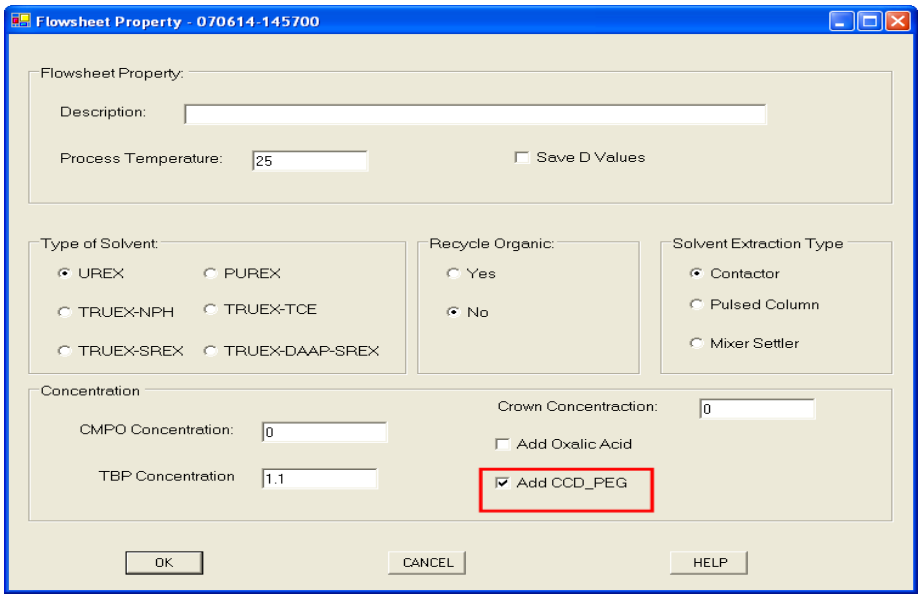

Figure 20: Interface for enabling/disabling the "CCD_PEG" module with the AMUSE simulator.

The Second ISOPro Program Revision

Stream display and updating issues have been corrected. Stream value display interface in the ASPEN-Plus Tree View Interface has been recoded for interactively displaying program execution status as shown in Figure 21. The newly recoded function can also display results accurately from the test "bkp" files created by the UNLV development team. For faster responding time, the interface validates the existence of any output data in the "bkp" file prior to retrieving all data sets.

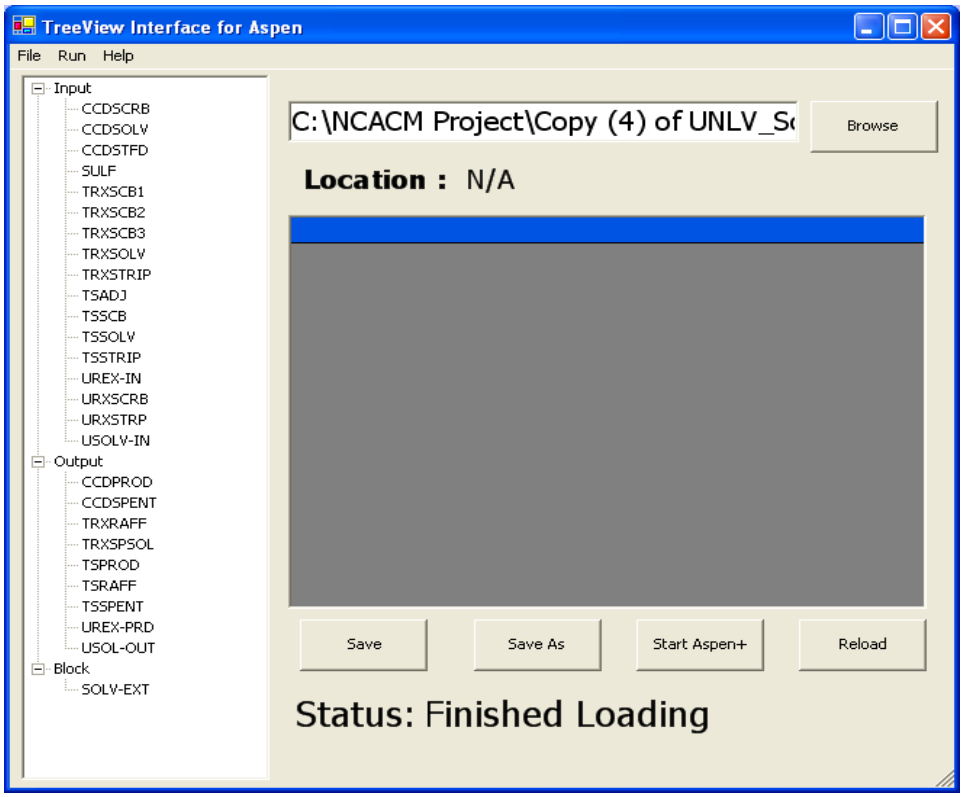

Figure 21: The revised ASPEN-Plus Tree View interface showing program execution status.

First Draft of ISOPro User Manual

The first draft of the ISOPro user manual was completed and includes: overview for both AMUSE-lite and ASPEN-Plus interfaces, acronyms and definitions associated with the ISOPro program, and explanation and screenshots for both interfaces. Three distinct test cases: ASPEN-Plus interaction, AMUSE simulation, and database result presentation demonstrate the capability of the ISOPro.

Electrochemical Separation of Curium and Americium (Task 25).

Room temperature ion liquids (RTILs) solutions have been successfully prepared, and the potential windows were previously measured (Figure 22). The electrochemical window for RTIL system is based primarily on the reduction of the cation and oxidation of the anion used to make the solution. The potential window is significantly larger for RTILs ranging from approximately 4.5 to 6 V when compared to aqueous environments. The potential windows obtained in aqueous solutions of 0.1 M H_2SO_4 (blue line) and the RTIL, tri-n-butylmethylammonium bis(trifluoromethylsulfonyl)imide ($[MeBu_3N][NTf_2]$, red line) at GC, Au, and Pt electrodes are illustrated in Figure 22. For each electrode the positive and negative potential limits provide an absolute potential window of approximately 4.5 V for Pt, 5.0 V for Au, and 6.0 V for GC. The base of RTIL cations has been extended to include immidazolium and have started obtaining background voltammetry consistent with Figure 22.

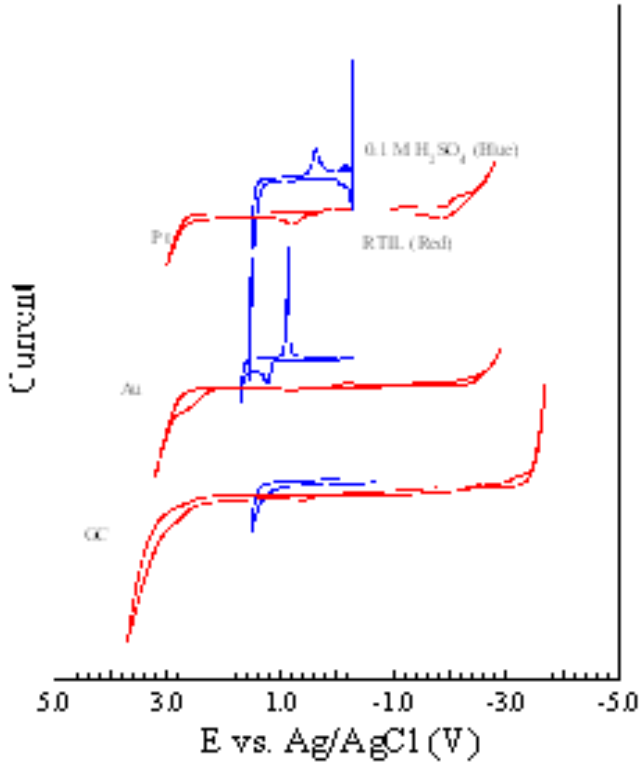

Figure 22: Electrochemistry of GC, Au, and Pt electrodes in RTIL ([$MeBu_3N$][NTf_2]), (red) and 0.1M H_2SO_4, (Blue).

The preliminary electrochemical characterization of Eu in RTIL ([$MeBu_3N$][NTf_2]) is show in Figure 23. The voltammery is characterized by the oxidation and reduction of Eu at negative potentials between 0 and -2 V. In addition, the electrochemical deposition of Eu(0) is observed electrochemically at a potential of ~2.5 V. The results demonstrate the ability to observe voltammetry for Eu that cannot be observed during aqueous electrochemical experiments. Studies of UO_2 and UO_3 in RTIL solutions have begun. The goal of these measurements is to identify the electrochemical characteristics of the species in the RTIL and evaluate the feasibility of tailored electrodeposition of Uranium species. $UO_2(OH)_2$ and $UO_2(N(Tf)_2)_2$ have been examined with decent resolution of the Uranium redox chemistry. These are preliminary studies which will continue to examine the species in RTIL solutions.

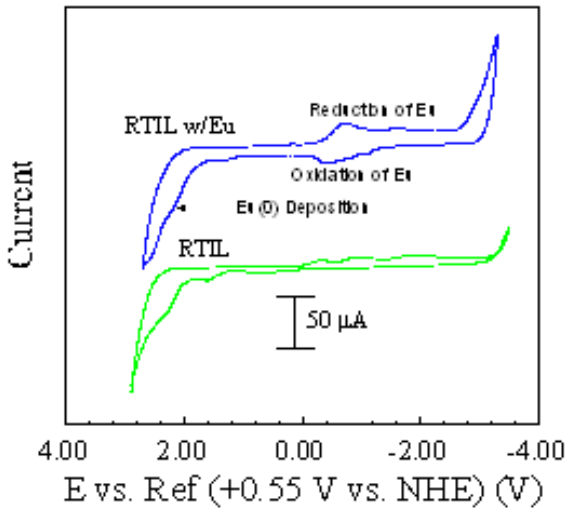

Figure 23: Electrochemistry of Eu at a Pt electrode in RTIL ([MeBu$_3$N][NTf$_2$]).

Fundamental Chemistry of U and Pu in the TBP-Dodecane-Nitric Acid System (Task 26).

Work continued on the extraction studies. More experiments were performed in order to evaluate how to use a liquid scintillation counter (LSC) as an accurate measure of uranium concentration. Also, titrations of previous samples were repeated since the data did not match previous samples. Studies also continued on uranyl-AHA structure and complexation as well as the speciation of Tc-AHA.

Uranium Extraction Studies - Sample Generation

Samples were made of an aqueous phase and an organic phase. The aqueous phase consisted of nitric acid, lithium nitrate, uranyl nitrate and water. The concentration of nitric acid was 1 M, and the total nitrate concentration varied by addition of $LiNO_3$. The amount of $LiNO_3$ ranged from 0 to 9 M. The uranium concentration investigated was 0.01 and 0.02 M $UO_2(NO_3)_2$. The organic phase of each sample consisted of a pre-equilibrated solution of 30% TBP (tributylphosphate) in dodecane. Volumes of 0.75 mL of each phase were contacted by mixing for 2 minutes with a vortexor. Then the samples were centrifuged for 3 minutes to ensure complete separation of the two phases. Each phase was extracted and stored separately. The analyses were run on both the organic and aqueous phases.

Uranium Extraction Studies - Acid Determination

The acid concentration of each phase was measured by titration on a Metrohm automated titrator. Figure 24 shows a plot of the acid extracted into the organic phase. There is an increase in acid being extracted with TBP as the amount of total initial nitrate increases. At these conditions, the amount of acid in the organic phase is not affected by the uranium concentration.

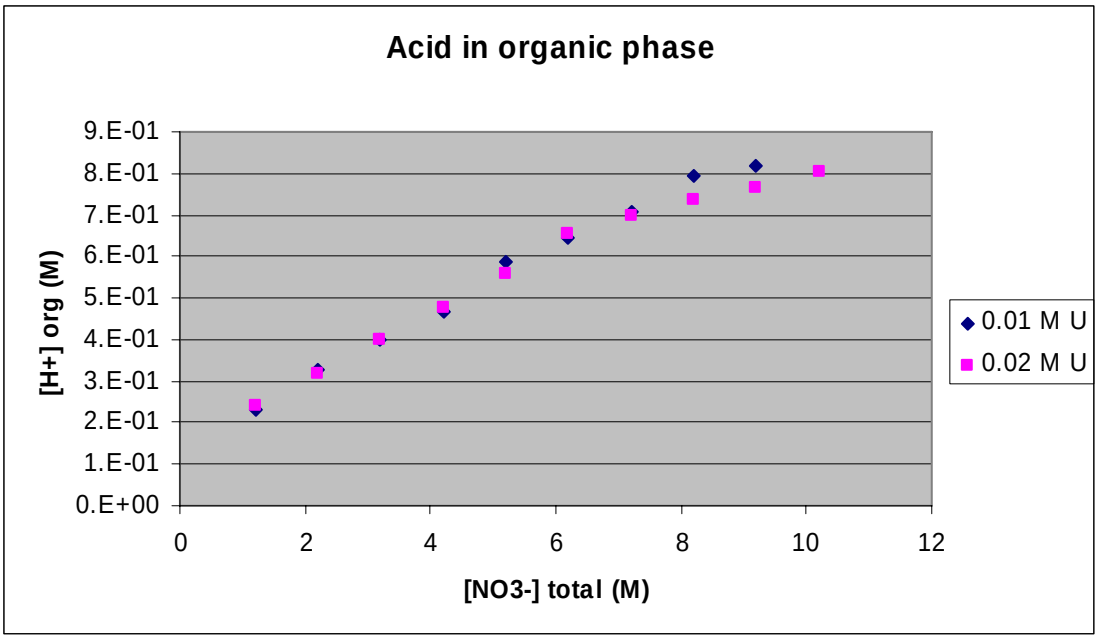

Figure 24: Acid extracted into the organic phase.

Uranium Extraction Studies - Uranium Determination

Experiments were run to compare uranium determination by LSC against ICP-AES. The difference between the results of the two methods dramatically decreased when uranium concentration was high, even though the low concentrations were above the detection limit of the LSC. Experiments were conducted to see if increasing the count rate decreased the difference in the two methods.

The samples were prepared with an aqueous phase consisting of uranyl nitrate at 1M. To one of the 1M solutions 1mL of 1500 Bq/mL of U-233 was added before extraction. The organic phase of each sample consisted of a pre-equilibrated solution of 30% TBP (tributylphosphate) in dodecane. Volumes of 0.75mL of each phase were contacted by mixing for 2 minutes with a vortexor. Then the samples were centrifuged for 3 minutes to ensure complete separation of the two phases. Each phase was extracted and stored separately. The analyses were run on both the organic and aqueous phases.

Dilutions in 1% nitric acid were made for ICP-AES analysis, and 100uL of each sample were placed in 10 mL of scintillation cocktail for LSC analysis. The results of the two methods differ by greater than 10%. The increased count rate due to ^{233}U did not seem to minimize this discrepancy.

U Acetohydroxamic Acid Crystal Structure

A method for obtaining amorphous solid UAHA was developed previously, and its product extensively characterized with available spectroscopic methods. Though several attempts have been reported at meetings and in the literature, the crystal structure of UAHA was unknown until recently.

The crystals were obtained from an initial solution containing 100 mM uranyl nitrate and 1M AHA, titrated to pH 1.2, and centrifuged to remove the immediate precipitate. The resulting 34 mM U solution was allowed to age for several months, at which point a crystalline orange material was obtained. The mother liquor contained approximately 1.3 mM uranyl and had a pH of 4.73, indicating that the AHA had hydrolyzed to its daughters acetate and hydroxylamine, which often further breaks down to water and nitrogen gas.

More information on the crystal structure is contained in the previous quarterly report. It is reproduced in Figure 25.

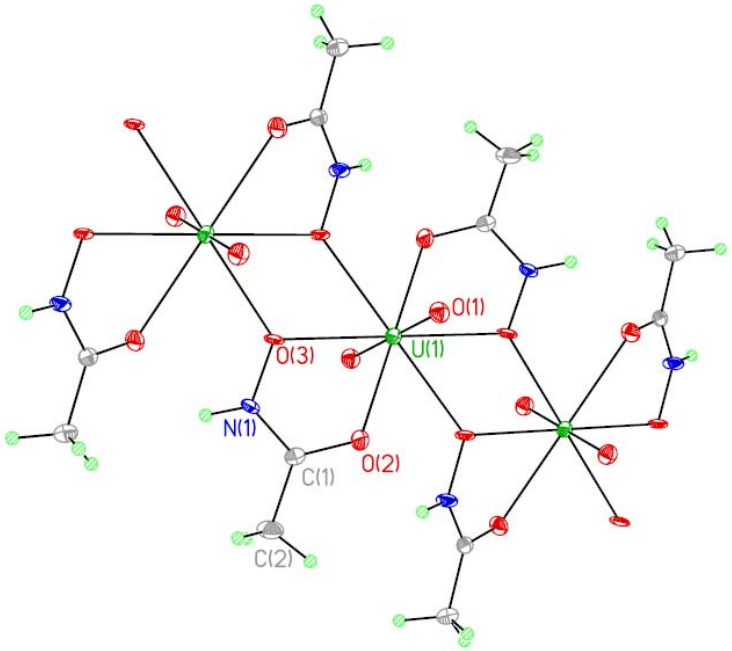

Figure 25: Crystal structure of uranium acetohydroxamic acid.

This is the first crystal structure of an f-element complexed to AHA, and only the second metal-AHA complex reported ($Fe(III)(AHA)_3$ was reported in 2000). The reason for this dearth of crystal structures is likely due to some combination of the following characteristics of AHA systems:

- AHA tends to polymerize.
- AHA breaks down in water, leading to pH changes, a decrease in ligand concentration, and an increase in competitors (acetate, hydroxylamine).
- AHA and its breakdown product, hydroxylamine, are powerful reductants.
- The hydrophilicity of AHA, which is a small ligand, and hydration of the ligand and metal centers make it difficult to crystallize the materials from aqueous solutions.

The UAHA complex is polymeric, though each unit cell contains two equatorial AHA ligands, as predicted from stoichiometry measurements and the binding of AHA. What was not predicted was the binding of the AHA ligand from neighboring U atoms to form the UAHA polymer. This

causes the AHA ligands to bend out of plane. In each ligand, one O is above the plane and the other below. Though the molecule is not square pyramidal, it has a high symmetry; all of the non-yl U-O bonds are 60 degrees from each other, as viewed from the yl axis, and the 30-degree bend out of plane means that they are 60 degrees from each other as viewed from any O-U-O axis. This crystal structure information is crucial in evaluating the complexation constant for the U AHA system.

U Acetohydroxamic Acid Crystal Structure – Evaluation of AHA pK_a

Equilibrium constants depend on the equilibrium concentration of each reagent and product, the stoichiometry of the reaction, and the activity coefficients of each component. These activity coefficients vary with reaction conditions and are highly dependent on both the ionic strength of the solution and the identity of the ionic salt; in an ideal solution of zero ionic strength, the activity coefficients of all the components equal one.

Ionic strength thus can have a huge effect on the measured acid constant (pK_a) values of a given molecule. Acetohydroxamic acid is small but has three ionizable functional groups: the hydroxyl O and amine N can give up or take up a proton, and the ketone can protonate. In practice the ketone does not act as a Brønstead base, and AHA can act as either an N- or O- acid, depending on conditions. A recent NMR study (*J. Org. Chem.* 2003, *68*, 6535-6542) indicates that the N gives up a proton before the O, but it may quickly isomerizes back to the hydroxide.

AHA is of interest as a simple model for humic acids as well as in the nuclear fuel cycle, and much research has been done on its fundamental properties. Surprisingly, its pK_a value has varied wildly in published reports, from as low as 8.7 to as high as 10.2. This value is incredibly important for modeling the stability constants of its metal complexation, as a one-unit change in pKa can result in a 1.3 unit change in β for a two-ligand complex (like UAHA), and a 2.4 unit change for a three-ligand complex (like FeAHA). In fact, the three published or presented UAHA stability constants vary from 13.5 to 14.7.

The literature pK_a values were reported over a range of ionic strengths, and often with no ionic strength mentioned. It is plausible that the effect on the pKa can be affecting the measured pK_as. Such an effect can be modeled using the Specific Ion Interaction Theory, (SIT). From the *Journal of Solution Chemistry,* Vol. 15, No. 5, 1986:

The fundamental result of the SIT is that the activation coefficient γ_I of ion j of a net charge z_j is given by

$$\log \gamma_i = -z_j^2 D + \sum \varepsilon(j,k,I) m_k$$

If the pKa of AHA is measured at various ionic strengths, its constants can be determined and modeling of the stability constant will be significantly more accurate.

Titrations were performed in aqueous media at 0.1, 0.3, 0.5, 1, 2, and 3 M $NaNO_3$ and 0, 0.005, 0.01, and 0.05 M AHA. The pKa of the blank (no AHA) was used as the pKw for modeling with Hyperquad. Each titration was performed in triplicate and the results averaged for modeling. The base was prepared by diluting 1.000 +/- 0.005 N NaOH (VWR) and a 5M $NaNO_3$ stock into

Millipore water (> 18 MΩ). The samples were prepared using the same 5M $NaNO_3$ stock and a freshly prepared 0.1 M AHA stock solution. The samples were titrated on the Brinkmann titrator. The data were fed into Hyperquad. The pKa values and fit were determined; a typical output file is shown in Figure 26.

```
Results page            Run timed at 12.48 on 30 May 2007
 0.3-0.005      3 iterations Refinement successful
 Chi-squared = 167.84
 Chi-squared should be less than 12.60 at the 95% confidence level
   sigma =     0.2508 Value     relative      log      standard
                                          std devn      beta     deviation
  Beta  -1  0    constant   1.6596E-14                -13.7800
 Beta    1  1    refined    1.7380E+09   0.0083        9.2401    0.0036     (
9.24005305616835     )
```

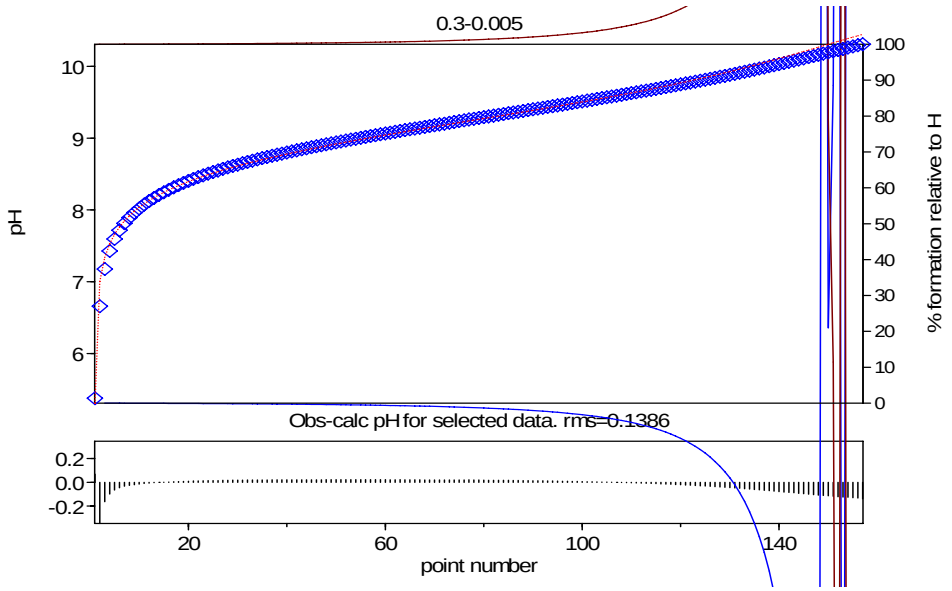

Figure 26: Typical Hyperquad output file.

The fits for most of the data points were very good. Some titrations had to be redone. The pKa values determined are summarized in Table 1.

Table 1. pKa values.

Ionic strength	pK_w	pK_a	pK_a	pK_a
0.1	-13.73	9.6000	9.3098	9.3446
0.3	-13.69	9.1735	9.2045	9.2401
0.5	-13.63	9.1445	9.1278	9.0618
1	-13.58	9.0287	8.9926	9.026
2	-13.47	9.3295	9.0227	9.0148
3	-13.56	9.1735	9.2045	9.2401

The outlying data points are more obvious when graphed as shown in Figure 27.

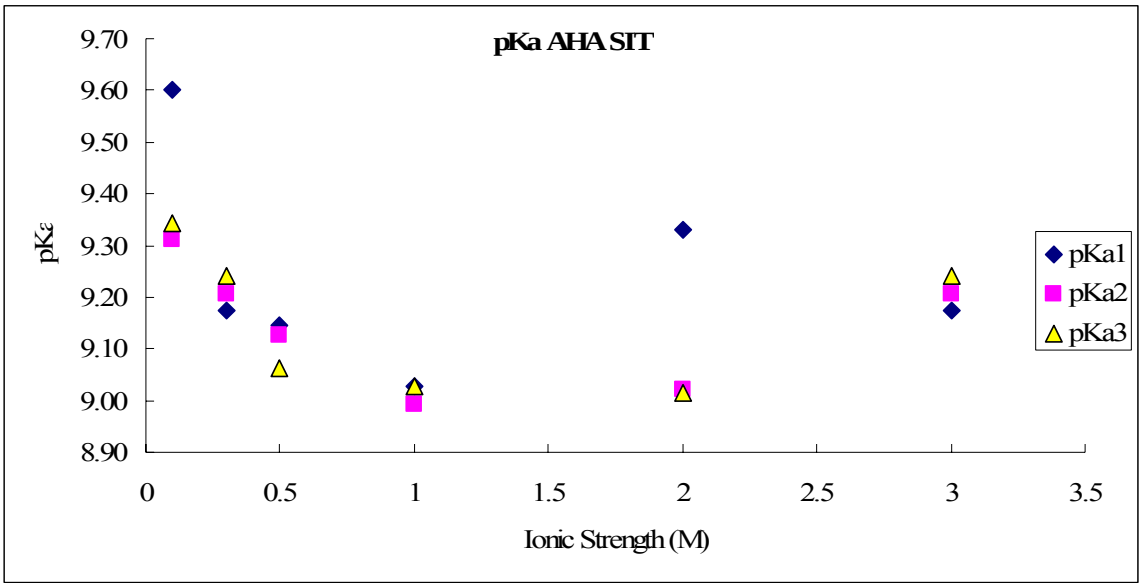

Figure 27: pKa values versus ionic strength.

They are both from the very low concentration of AHA. The resulting data will prove useful in evaluating the complexation constants for U with AHA, comparing the data to the existing literature collected over a range of ionic strengths.

Speciation of the Tc-U-AHA System

The reduction potentials of Tc(VII)/Tc(IV) and AHA/breakdown products indicate that it is theoretically possible to reduce pertechnetate to Tc(IV) using AHA. This may alter the fate of technetium during the extraction process. Despite several literature conclusions that AHA does not reduce Tc(VII) during recovery conditions, it was found that under conditions that deviate only slightly from UREX+ conditions (1.0 instead of 0.6 M AHA), AHA does in fact reduce pertechnetate and form Tc-AHA. In the previous report, the exact nature of this compound was unclear.

In the previous report, the effect of AHA on extraction was reported. Upon further study, it seems that at least part, if not most, of the effect was due to the change in pH as AHA breaks down and not on the formation of TcAHA. The production of TcAHA was studied as a function of acid, technetium, and AHA concentration in nitric and perchloric acid. The resulting products were compared to those formed by hydroxylamine. The studies were performed at 20 and 30 C. The synthesis of TcAHA is greater at accelerated temperatures. The final product is at pH 4.72 due to the production of acetate.

The red TcAHA complex can be made from TcO_2 (amorphous) in a 4 M AHA solution. Mixing wet, amorphous TcO_2 with 10x molar excess solid AHA releases enough water to dissolve the resulting compound (est. >2M Tc, no precipitate). A spectrum of the complex diluted into pure

water shows it to be a brown-black compound whose spectrum diminishes measurably with time. Addition of enough AHA to bring the final solution to 4 M, then waiting overnight, turned the complex wine-red. UV-vis showed that this complex is the same as the one previously obtained. Wayne Lukens of LBL has obtained EXAFS data of this compound, but has not yet fully analyzed the data. Material is in the freezer for when the freeze-dryer is functional. An attempt will be made to purify it and take IR/NMR.

Speciation of the Tc-U-AHA System - Characterization

It was determined by EXAFS that the product is a technetium-nitrosyl (TcNO) complex, one of about a dozen now known. It is the first TcNO complex reported directly from pertechnetate; often $TcCl_6^{2-}$ or $TcNOCl_5^{3-}$ are used as starting materials. In addition, this synthesis uses AHA as the nitrosyl source. The first reported TcNO complex used hydroxylamine, a breakdown product from AHA, as its source, but most work uses NOCl, HNO, or NO gas as a source of NO. The electron paramagnetic resonance spectrum reveals a d^5 compound, so the complex is Tc(II).

Speciation of the Tc-U-AHA System - Spectroscopy

The basis spectrum of the complex as shown in the previous report (below, in red in Figure 28) was incorrect. In Figure 28, the correct basis spectrum is presented in blue.

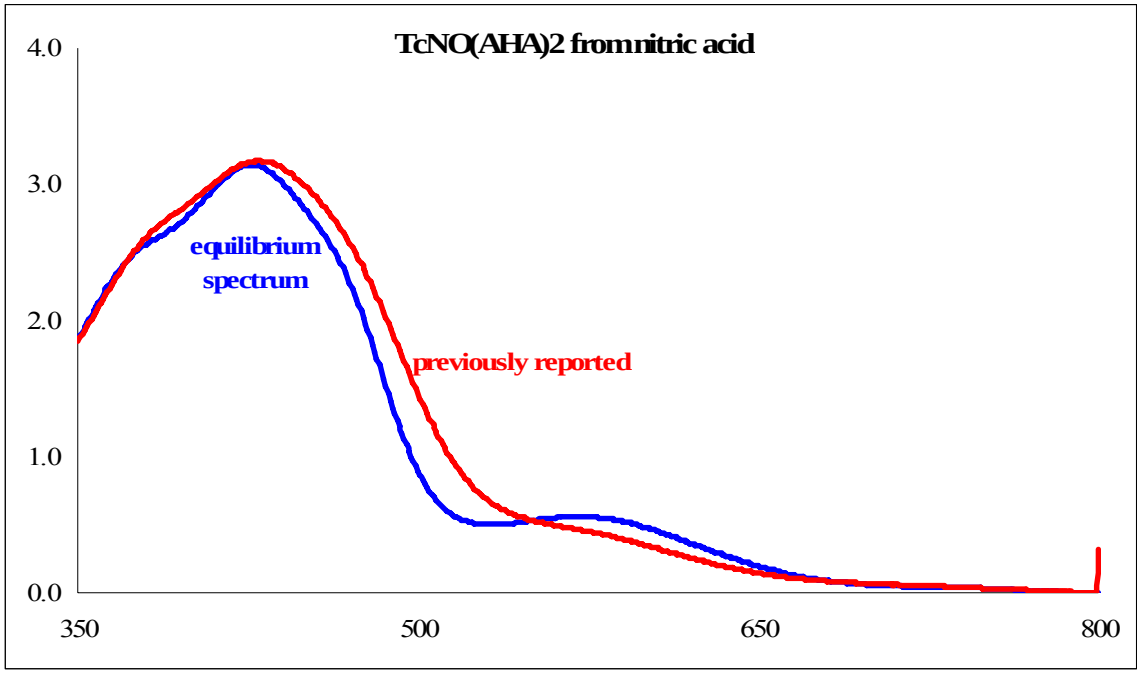

Figure 28: Basis spectrum of $TcNO(AHA)_2$ from nitric acid.

The strong absorbance of nitrate below ~340 nm prevents the measurement of the rate of decrease of pertechnetate in that medium.

Speciation of the Tc-U-AHA System - Effect of Temperature

The rate of formation of TcNOAHA, as measured by the peak absorbance at 427 nm, is approximately 3 times faster at 30 C than at 20 C as shown in Figure 29. The exception is at 1 M AHA; it appears that the data at 20 C did not fit the trend.

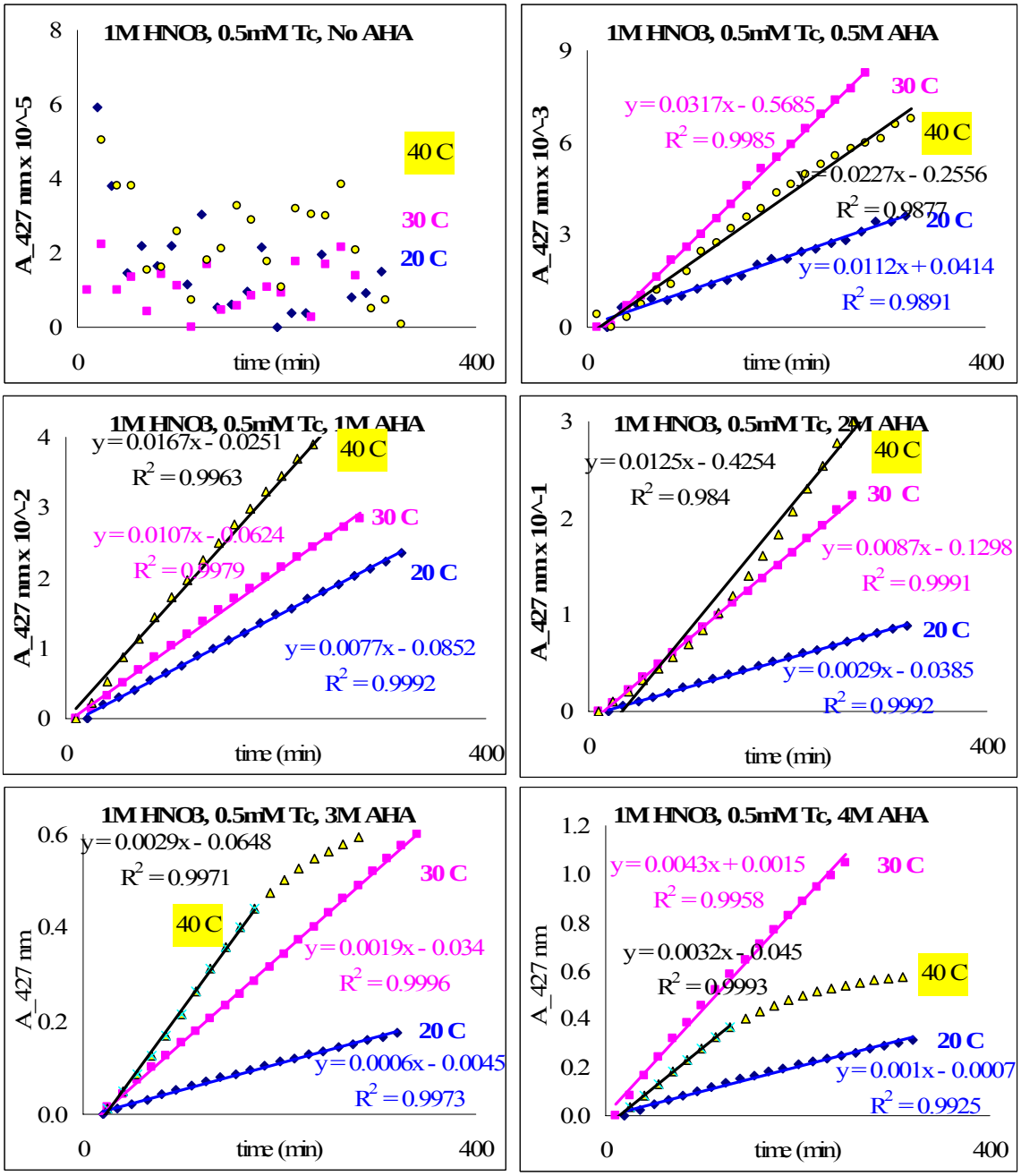

Figure 29: Formation of TcNOAHA at various temperatures.

The data at 20 and 30 C deviate from linearity after approximately 5 hours. Note that the rate at 30 C is approximately three times that at 20 C. For the 40 C information, it seems likely that the AHA is just breaking down before the reaction can occur, changing the pH and the ligand concentration. There was a strong smell of acetate when the material was harvested.

Speciation of the Tc-U-AHA System - Proposed Mechanism

AHA has been reported as a 1- or 2- electron donor.

AHA → acetic acid + ½ N_2 + H+ + 1 e-
$2H_2O$ + AHA → acetic acid + $HN(OH)_2$ + 2H+ + 2e-

Having two possibilities for reduction makes it difficult to determine the correct route. In addition, bubble formation could be from N_2 gas or from heat, radiolysis, or vaporization of water. A preference for the 2e- donor is based on the observation of bubble formation when concentrated AHA is in the presence of 2M or greater HNO_3, but not many bubbles were found in the Tc experiments.

Proposed mechanisms:

1. Preequilibrium:
    a. Step 1, equilibrium: TcO_4^- + HAHA + H^+ ↔ $TcO_3(AHA)(H_2O)$ octahedral complex with K = $[TcO_3(AHA)(H_2O)] / [TcO_4^-][AHA][H^+]$
    b. Step 2, irreversible reaction: $TcO_3(AHA)(H_2O)$ + HAHA → $TcO_3(AHA)(H_2O)^-$ + $1/2N_2$ + H^+ + CH_3CO_2H, rate = k
    c. Subsequent steps very fast: $TcO_3(AHA)(H_2O)^- \rightarrow \rightarrow Tc(NO)(AHA)_2)(H_2O)^+$
    d. Rate: $d[Tc(II)] / dt = -d[TcO_4^-] / dt = k[HAHA][TcO_3(AHA)(H_2O)] = kK[TcO_4^-][AHA]^2[H^+]$

2. Disproportionation:
    a. TcO_4- + AHA + 4H+ → acetate + $Tc(V)O^{3+}$ + H2O + $HN(OH)_2$
    b. $3Tc(V)O^{3+} + H_2O$ → $2Tc(IV) + TcO4^- + 2H^+$
    c. Tc(IV) + AHA → $TcAHA_2$ (observed)
    d. $Tc(AHA)_2 + H^+$ + AHA → acetic acid + $TcNOAHA_2^+ + H_2O$
    or $Tc(AHA)_2$ + HNO3 → $TcNO(AHA)_2$ + H2O

Speciation of the Tc-U-AHA System - Addition of Uranyl

Uranyl was added to the system to determine its effect on the reduction of pertechnetate, and on the extraction characteristics. Two variables were studied, AHA and uranium. In all cases involving Tc, its concentration was held constant at 0.5 mM. UO_2 controls were performed without Tc. [Tc] was measured by LSC and [U] by Arsenazo. Solutions were prepared in the plastic 1.5mL cuvettes. Acid was added, time noted, and cuvettes were capped tightly. Temperature was maintained and spectra were obtained.

The extinction coefficient of UAHA is an order of magnitude lower than that of TcNOAHA, but when present in 20x excess (10mM U, 0.5mM Tc) the UAHA absorbance almost completely obscures that of the TcNOAHA. Comparison to UAHA (No Tc) and TcAHA (No U) controls for the rate of increase at certain wavelengths gives an estimate of how much the presence of U affects the rate of TcAHA formation.

There was no effect of uranyl on the extraction of technetium into 30% TBP, though the effect of the AHA concentration was still observed as shown in Figure 30.

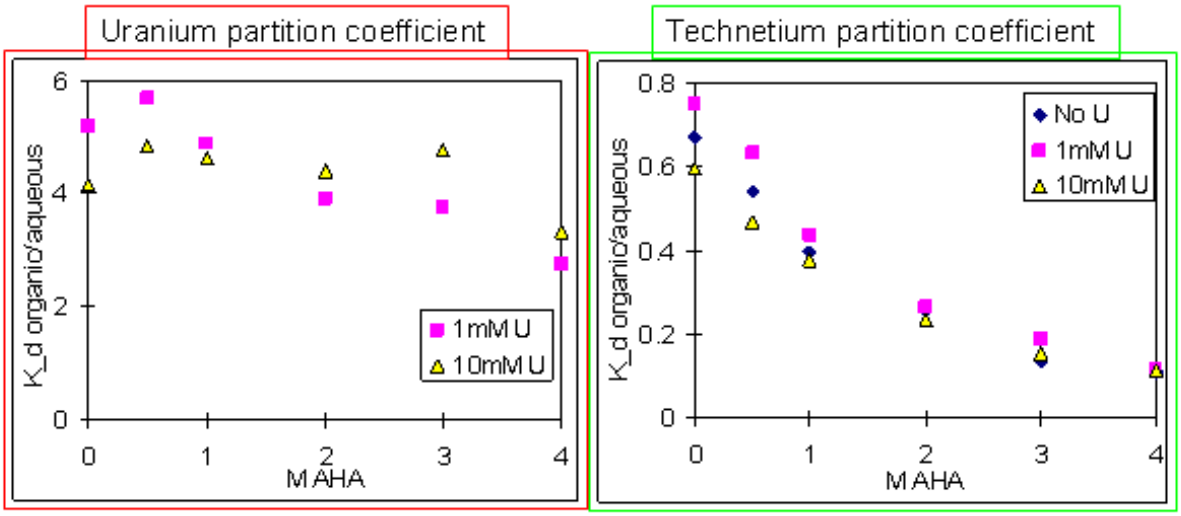

Figure 30: U and Tc partition coefficients as a function of AHA concentration.

Figure 31 shows the increase in the 427 nm peak absorbance as a function of time at 20 C. Samples tested were all 1M HNO_3; those with Tc had 0.5mM NH_4TcO_4 at the start. The equation for the rate of increase in the linear range can be solved and the slopes (rate of increase in the absorbance at 427 nm) can be determined as a function of AHA concentration for Tc with and without U, and for U without Tc.

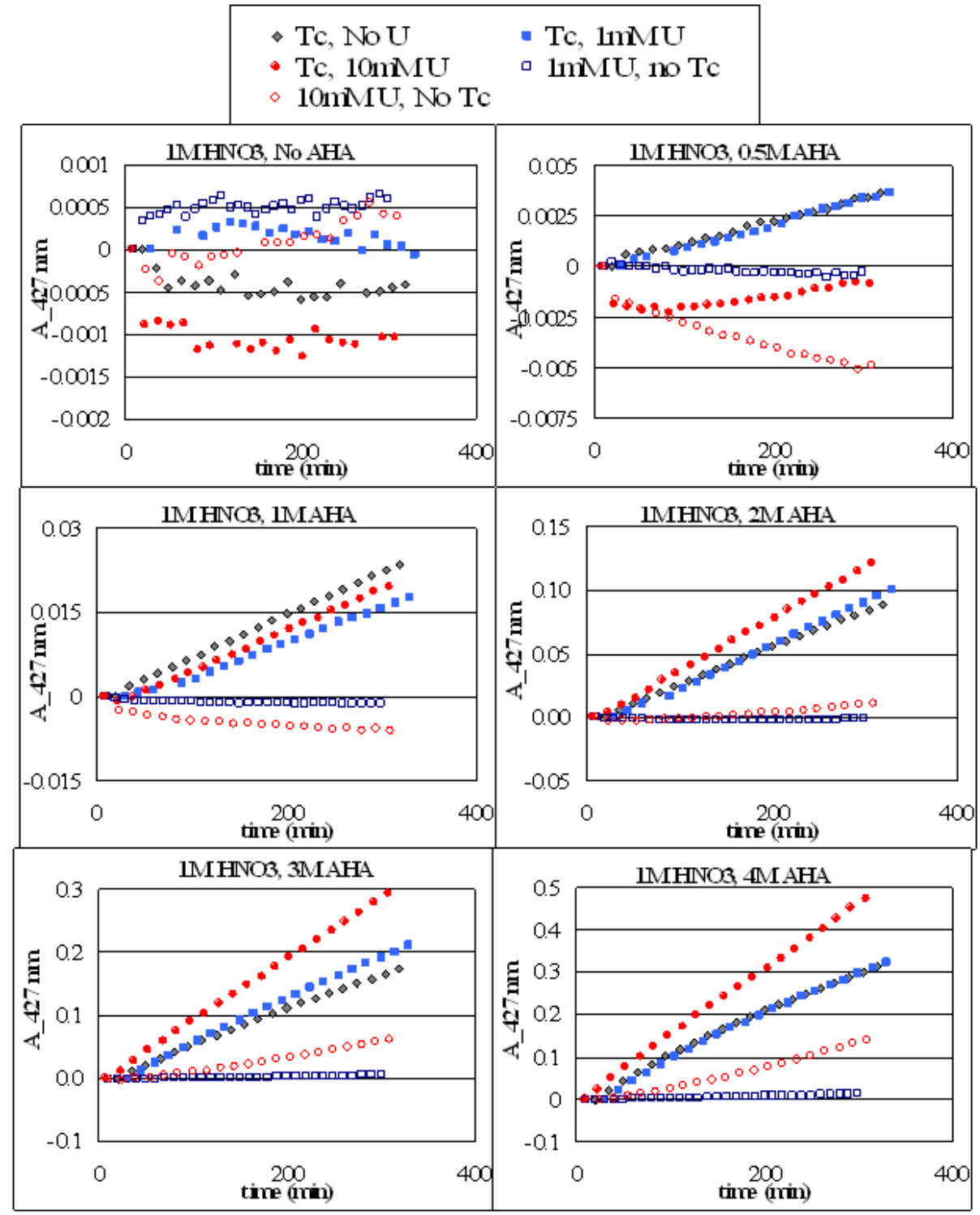

Figure 31: The 427 nm peak absorbance as a function of time at 20 C.

The effect of U was corrected for by subtracting the rate of 1mM U alone from the rate with 0.5mM Tc/1mM U; the same was done for 10mM U (Figure 32).

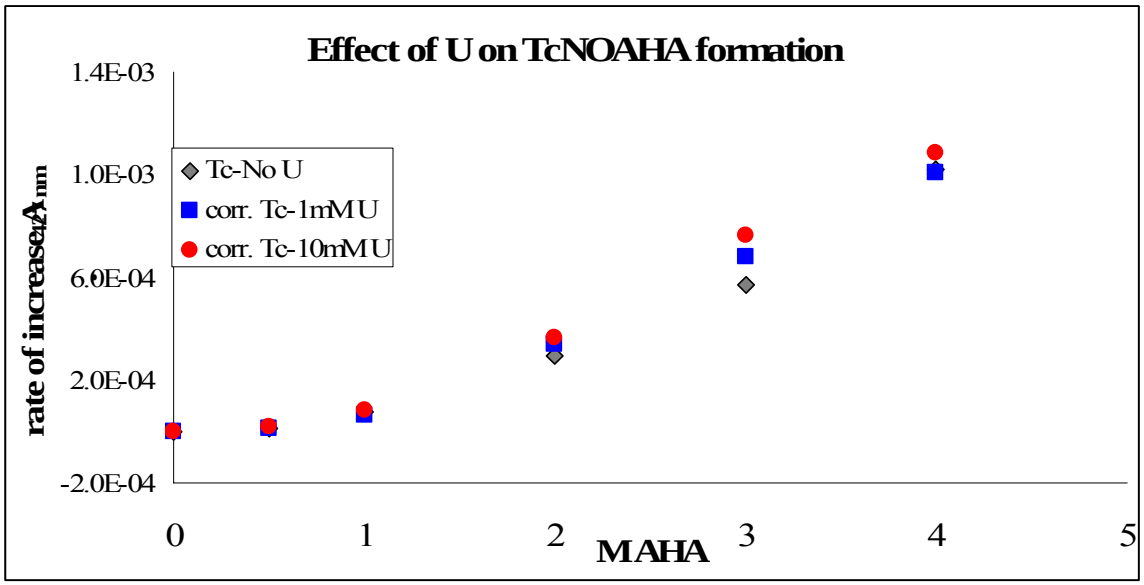

Figure 32: Effect of U on TcNOAHA formation.

These data suggest that there is a negligible effect of the presence of uranyl on the formation of TcAHA. The strong smell of acetate when the solutions are uncapped indicated that the pH increase due to acetate formation could be having a severe effect on the absorption spectra as well as the extraction. UAHA formation is generally instantaneous, and when the pH is buffered no change in spectra are seen. However, there is an effect of pH (see last quarterly report). This suspicion was intensified after it was determined that while the concentration of uranyl has no effect on the extraction of technetium by 30% TBP, the temperature that the experiment was run at dramatically changed K_d for both U and Tc, even though the extractions were performed at the same temperature. A quick examination of the extraction of ammonium pertechnetate from 1 M HNO3 and 150 mM NaOAc buffers confirmed this suspicion as shown in Table 2.

Table 2. K_d measurements using liquid scintillation counting.

Kd	immed	24 hours
pH 4	0.014	0.051
pH 5	0.011	0.040
4M AHA	0.422	0.013
1M HNO3	0.881	0.952

K_d is measured via liquid scintillation counting and is calculated by dividing the number of counts per volume from the organic phase by the counts per volume of the aqueous phase. These numbers were correlated well with those calculated from the difference of the initial and post-extraction aqueous phases.

To determine the effect of TcAHA partitioning in the absence of UAHA and at 1 M HNO_3, 400 uL of the original solutions with Tc and 4 M AHA were taken after 2 days and diluted with acid and water to 1 mL for a final concentration of 1 M HNO_3. Aliquots were extracted and the spectra were measured.

Uranyl-AHA hydrolyzes at such high acid concentrations, and the TcAHA was visible after the UAHA spectra were destroyed. The spectra were normalized to the number of counts in each sample to correct for differences in Tc. It is fairly clear that TcAHA formed to the same extent regardless of uranyl concentration, indicating that, at least in 4 M AHA, the thermodynamic product is independent of uranyl interference.

The increase in absorbance for 20 and 50 mM U in Figure 33 is due to the absorbance of free uranyl, as indicated by the characteristic line structure between 350-500 nm. The re-acidified samples do indicate an effect of uranyl concentration on the extraction of Tc from 4M AHA. The uranyl assay may be unreliable at initial concentrations below 10mM because of the sensitivity of the Arsenazo(III) test at the concentrations of the dilutions.

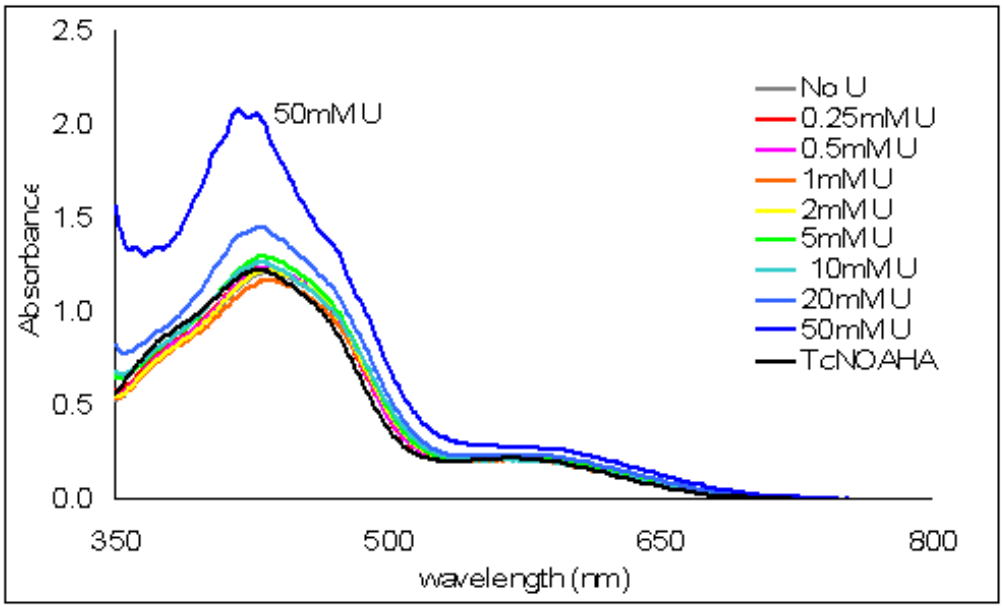

Figure 33: Absorbance for various concentrations of U.

While there is now a small effect of uranyl on Tc K_d, it is also worth noting that the values of the distribution coefficients are an order of magnitude lower than before the HNO_3 was added, indicating that TcAHA, in the presence of free uranyl and at 1M HNO_3 as would be encountered in a UREX-type system, does not extract into 30% TBP.

Investigation of Optical Spectroscopy Techniques for On-Line Materials Accountability in the Solvent Extraction Process (Task 29).

Determination of Uranium Concentrations by Laser Fluorescence in the Aqueous System

To evaluate the potential utility of laser fluorescence spectroscopy (LFS) for the determination of uranium concentrations in the aqueous process streams, it is necessary to understand how the other components in the process stream may impact the fluorescence behavior. In addition to the fission products and transuranic elements from the used nuclear fuel, the process streams will also contain the corrosion products from the degradation of the plant hardware. Of the degradation and fission products present in the feed stream of the UREX process, iron is present in the largest concentration (~150 mMol/L).

At a given concentration of uranium, ~500 µMol/L, increasing amounts of iron (III) perchlorate were added in a perchloric acid medium (pH~1). The results are shown in Figure 34, plotted as the Integrated Total Fluorescence (ITF) vs. the iron concentration.

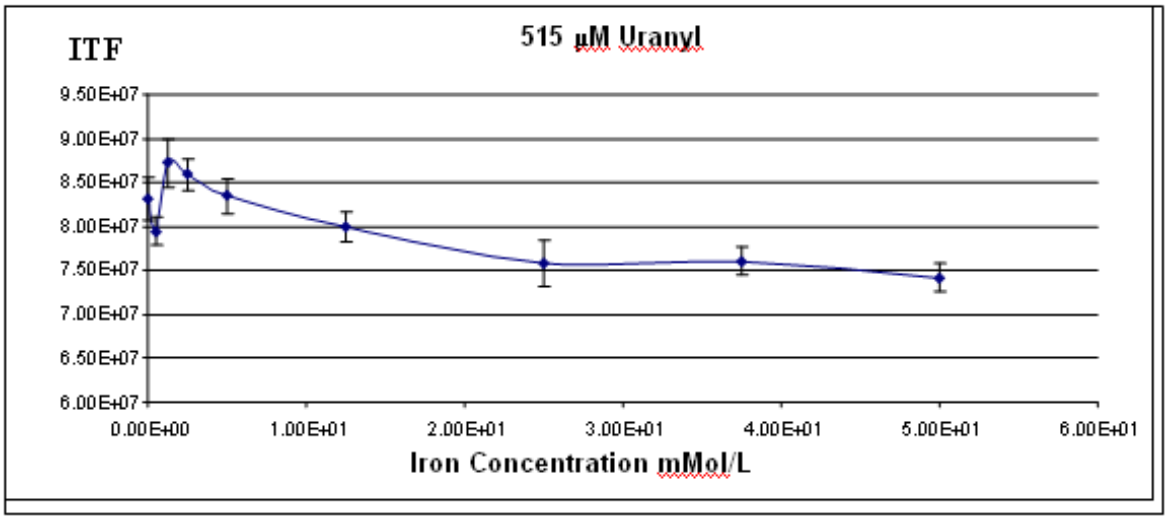

Figure 34: Integrated Total Fluorescence (ITF) as a function of iron concentration.

Figure 34 shows a decrease in the fluorescence yield expected of a quenched system. However, at this point, the total decrease is less than 10% of the maximum fluorescence. Work will progress in the next quarter to extend these experiments out to cover the expected concentration range in the process.

Determination of Uranium in the UREX Organic Streams by UV-Visible Spectroscopy

The investigation of UV-Vis spectroscopy for determining uranium concentrations in the organic streams continued this quarter. To properly evaluate the molar absorbtivities and determine detection limits, the first step was to develop calibration standards. Given the potential impact of the chemical environment on the absorption spectrum, the standards had to be prepared in the organic system free of an aqueous fraction. Methods for preparing these standards were developed, and the concentrations in the standard solutions were verified against known standards directly by liquid scintillation counting of the organic matrix standards as well as indirectly ICP-AES on the aqueous fractions used to make the organic matrix standards (to confirm mass balance). These standards, and the corresponding methods, are to be used to

evaluate the impact of process conditions on the spectral behavior of uranium in the organic stream.

Combined Radiation Detection Methods for Assay of Higher Actinides in Separation Processes (Task 30).

The development of concepts and models continued for use of the ^{3}He Neutron Multiplicity Detector System (NMDS) for Materials Protection, Accounting, and Control (MPAC). Neutron slowing down spectrometers (SDS) were modedled and plans developed to conduct experiments at ISU with their carbon-based SDS (CSDS). This work will be used to investigate technology for assaying fuel rods and/or complete assemblies. In preparation for these experiments, MCNPX has been used to model neutron transport characteristics in LSDS and CSDS. The energy of neutrons measured in a neutron detector with an SDS can be characterized by the equation:

$$E = K/(t+t_0)^2, \text{ where K and } t_0 \text{ are characteristics of the SDS}$$

However, the detector system must be able to resolve the time dependence of the neutron signal. Because ^{3}He detectors, such as those contained in the NMDS, have a slow response, SDS configurations must be studied before conducting experiments. Those studies are currently ongoing, beginning with benchmarking computational methods. A Los Alamos National Laboratory LSDS was modeled to benchmark computational methods for determining energy-time correlation constants (Figure 35), and energy-time correlation constants, (Table 3), are now close to those obtained in LANL experiments. The next step will be to use the MCNPX code to design an experiment using the ISU CSDS and electron linac, followed by experiments conducted at ISU in the next year. Plans are being developed to conduct experiments at ISU with the CSDS to develop technology for assaying fuel rods and/or assemblies.

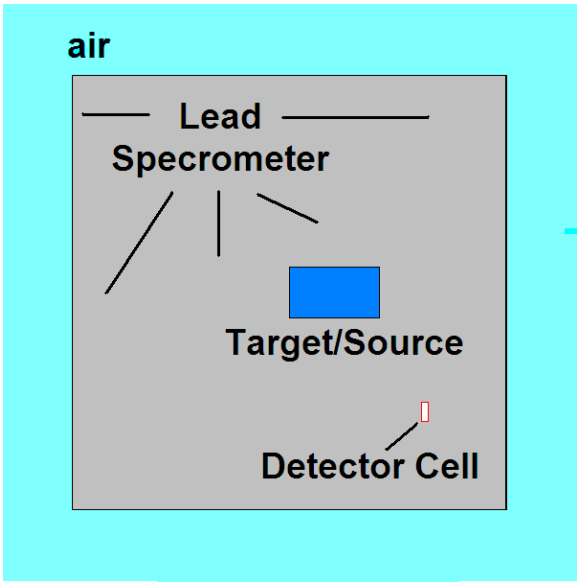

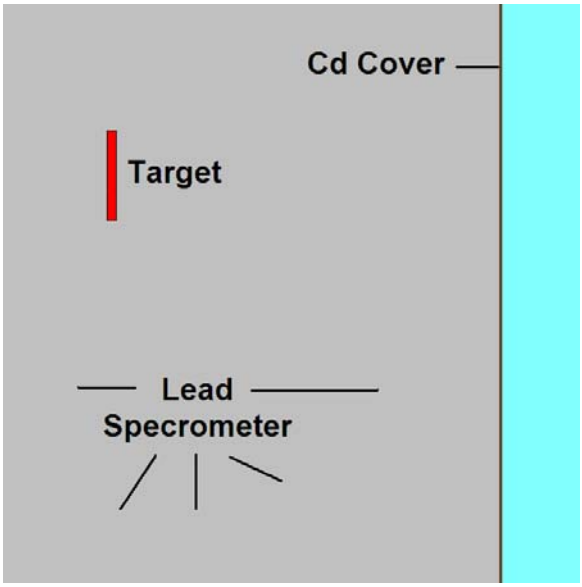

Figure 1a *Figure 1b*

Figure 35: Cross sections of the UNLV benchmark of the LANL LSDS taken from MXNPX models. (1a) the overall geometry, (1b) a close-up of a cross section of the thin target. The response to neutrons of various energies (time constants) is influenced by the position and isotopic composition of the detector.

Table 3: Comparison of UNLV MCNPX computed time constants versus LANL's values for the LANL LSDS benchmark.

Isotope	Resonance energy (eV)	K (keV*μsec^2) LANL	K (keV*μsec^2) UNLV
In-115	1.5	164	
Ta-181	4.3	161	148
Au-197	4.9	158	194
Ag-109	5.2	161.5	191
Ta-181	10.4	162	153
Ag-107	16.3	162.5	166
Cd-111	27.5	163	167
Au-197	59	159	174

Another application of NMDS to MPAC might utilize the measurement of both passive and active neutron multiplicity in very dilute concentrations of higher actinides, such as in a non-actinide waste stream. Currently, task members are investigating the applicability of the NMDS to measure quantities and isotopic constituents in such a stream. In addition, the NMDS is being upgraded to improve its performance. The upgrade included replacement of standard cables with coaxial cables to reduce electronic noise (background counts). Mapping of detector response with data collection and analysis software has been initiated by the students.

In addition to ongoing work, several new collaborations were initiated for upgrading and using the NMDS for safeguards and MPAC including an agreement with the V. G. Khlopin Radium Institute to upgrade and perform maintenance on the NMDS.

Synthesis and Properties of Metallic Tc and Tc-Zr Alloys as a Radioactive Storage Waste Form to Stabilize the Tc Waste Stream of the UREX+1 Process (Task 33).

The efforts in this quarter examined a larger scale elution experiment. A 150 mL solution of 0.01 M nitric acid were poured in a 250 mL ethylene bottle. Then $UO_2(NO_3)_2,6H_2O$ was weighted and added to obtain a concentration of uranium element between 50.03 g/L and 98.95 g/L. Finally NH_4TcO_4 was introduced in the mixture to obtain a concentration of technetium element between 66 mg/L and 360 mg/L. the solution was agitated before using. The anion exchange resin which was used was Reillex HP. However, this resin was treated in several ways to optimize its elution properties. During this work, seven resins were studied: six were treated and one untreated as shown in Table 4.

Table 4: Different types of resins used for the kinetic study.

Name	Initial resin	Type of treatment	Time of treatment
Resin 1	Reillex	Soaked in concentrated HNO_3*	12 days
Resin 2	Reillex	Heated** in concentrated HNO_3	3 hours
Resin 3	Reillex	Heated** in concentrated HNO_3	1 hour
Resin 4	Reillex	Soaked in concentrated HNO_3*	1 day
Resin5	Reillex	Soaked in concentrated HNO_3*	3 days
Resin 6	Reillex	Heated** in concentrated HNO_3	6 hours
Reillex	Reillex	None	/

* The concentration of nitric acid is 15.8 M

** The temperature for the heat treatment is 85 - 90 C

Static Experiments

Static experiments were carried out with the aim of determining Tc absorption capacity and elution properties of treated resins. In these experiments, seven different resins were studied. Each sample consisted of 100 mg of resin. These resins were placed in a 20 mL glass scintillation vial and conditioned in 10 mL of 0.01 M HNO_3 for one day before the experiments.

After conditioning, the aqueous solution was removed and 8 mL of water, 1 mL of 0.1 M HNO_3, 1 mL of a 1.23 x 10^{-4} M TcO_4^- solution were added in the vial. The kinetic study was running for 24 hours, during this time vials were shaken using a VWR DS 500 orbital shaker, with a speed of 50 rpm. The variation of Tc concentration in solution was studied as a function of time by liquid scintillation analysis using a Tri-Carb 3100TR. For this, 100 µL samples were taken at different times: 5, 10, 15, 25, 45, 100, 160, 240, 400 and 1440 min and added to 10 mL of scintillation cocktail.

After conditioning, the aqueous solution was removed and replaced by 8.045 mL of water, 1 mL of 0.1 M HNO_3 and 55 µL of a 0.189 M TcO_4^- solution. After 24 hours of sorption, the solution was removed, and 10 mL of 1M NH_4OH (eluting solution), was added to the resin. The kinetic elution study was run for 1 hour. During this time, 100 µL samples were removed at different times (1, 2, 3, 4, 5, 6, 7, 8, 9, 10, 15, 20, 25, 30 and 60 min), and added to 10 mL of liquid scintillation fluid to determine Tc concentration.

Dynamic experiments

Dynamics experiments were performed on simulated UREX solution in order to determine the separation factor U/Tc and to study the possibility of a Tc elution from the resin. Before carrying out a large scale experiment the influence of flow rate and concentration of eluting solution was examined. These experiments were performed using a one column set-up. Static experiments have shown that untreated Reillex has good absorption properties. Then, it was decided to use a two column experiment to improve the U/Tc separation. In this set-up, the last column contains the untreated Reillex resin. The one column and two column set ups and related procedures are described below.

The one column experimental set-up consisted of a reservoir of 250 mL, linked to a peristatic pump, with a constant flux which can be between 1,2 mL/min to 8,4 mL/min, itself connected to a small column (L = 5 cm and ø = 1 cm) contained 1 g of resin (Reillex HP or Resin 6). The process is divided into 3 steps: absorption, washing, and elution. For absorption, 150 mL of the UREX solution, were placed in the reservoir and pumped with a peristaltic pump through the column at a constant flow rate (2, 4 or 8 mL/min). Samples were collected into centrifugation tubes (45 m ± 0.5 mL for the first two and 10 mL ± 0.2 mL for the others. For each sample, 10 µL of solution were removed and mixed with 10 mL of liquid scintillation fluid in a plastic vial and ^{99}Tc was counted by liquid scintillation.

System was washed with 150 mL of ultra pure water until that the yellow color due to the uranyl nitrate disappeared and that the activity inside the centrifugation tube was about the background activity. Samples were collected into centrifugation tubes of 10 mL ± 0.2 mL or 45 mL ± 0.5 mL for the last ones.

The samples were eluted with a 50 mL solution of NH_4OH (1M or 2 M) and were introduced in the reservoir and poured through the column with the same constant flow rate. Samples were collected into centrifugation tubes of 10 mL ± 0.2 mL with 10 µL of samples were removed and mixed with 10 mL of liquid scintillation fluid for ^{99}Tc analysis. For sample containing a high amount of technetium, a dilution (1/100) was necessary for the liquid scintillation analysis, in order to be able to use the calibration curve. In order to optimize U/Tc separation, treated and untreated resin were combined. The set-up is composed as before by a reservoir, a pump and two columns, shown in Figure 36.

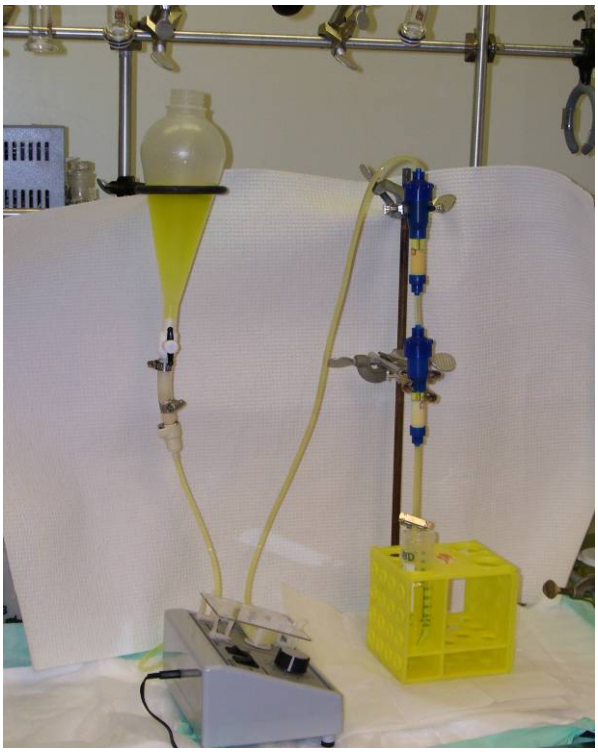

Figure 36: Experimental set-up with 2 columns.

The absorption and washing steps were carried out with exactly in the same conditions, as presented above. Concerning the elution step, the columns are disconnected and only the first one containing the treated resin is eluted, whereas the second one is kept for a re-use and for an eventual Tc reprocessing by pyrolysis.

Evaluation of Cs/Sr Waste Form for Long Term Storage and Disposal (Task 36).

In collaboration with the ANL team, the sample matrix shown in Table 5 for the material-waste form interaction experiments was developed. The potential container materials for the testing were down-selected to carbon steel and 316 L stainless steel for the primary candidates, with limited testing of higher cost options (Inconel 617 and Zircaloy-2) included as alternates. Procurement of the sample heats of the steels, as well as the cold chemicals and bentonite matrix materials was initiated. Method development for the microscopy of the steel/waste form interface has started, with method development to progress in parallel with the sample exposures.

Table 5: Testing Matrix: Carbon Steel and 316L SS.

Temperature	**Exposure Times**			
40 °C	1 month	2 month	3 month	6 month
150 °C	1 month	2 month	3 month	6 month
300 °C	1 week	2 week	3 week	4 week
450 °C	1 week	2 week	3 week	4 week

At each time/temperature combination, 4 samples will be prepared. The first is the control sample (no ceramic). The second sample has the metal test specimen in contact with the ceramic specimen. The third and fourth samples will be metal test specimens in contact with the ceramic which have been pressed at 2 different pressures to maximize the contact between the materials.

Due to the high cost of materials, only a limited test matrix will be pursued initially for the Zircaloy and Inconel samples. Only the 40, 300, and 450 C temperatures will be prepared, at only one contact pressure (as well as the static contact sample).

TRANSMUTATION SCIENCES

Corrosion Mechanisms and Kinetics of Steels in Lead-Bismuth Eutectic (Task 18)

Efforts focused on three tracks:

1. Development of local capabilities for LBE experimentation
2. Fundamental models of LBE corrosion of steels
3. Collaborative efforts

Laser micro-Raman capaility was developed in which a laser beam is focused (with spot size of ~2 micron) onto a sample of corroded steel. The spectra of the scattered light include information on the vibrational frequencies of the materials' components. Thus, the difference between chemical species (e.g., between Fe_2O_3 and Fe_3O_4) can be distinguished. This information complements other analytical techniques (e.g., XPS, EDAX) which are sensitive to the elemental composition and the oxidation state of the sample. In this reporting period, the apparatus was greatly improved by installing a spatial filter with improved spatial resolution and reduced danger of sample degradation. A recently obtained peak-fitting program has improved the analysis of the data, obtaining peak positions, widths, and associated uncertainties.

Simultaneously, this task is moving to establish the ability to calculate the Raman spectra of spinels and other relevant compounds. Collaboration has been initiated with Professor Kathleen Robins, a UNLV chemistry professor in theoretical physical chemistry. Robins will provide theoretical support for the experimental Raman program.

Construction of the Liquid Metal Test Facility continued during this period. Work using gas phase oxidation of structural steels to understand the differences between LBE corrosion of steel and gas phase corrosion has continued. Recently, a KALLA laboratory Oxygen Control System (OCS) was brought into operation – this will allow H_2/H_2O mixtures to be used to set oxygen potentials to the region where oxygen controlled LBE corrosion occurs.

Gas phase results led to questioning the role that water/hydrogen plays in the LBE corrosion of steel – the oxidation rate in LBE is so high that are some extra species expected to be serving the role of oxygen transport/storage medium.

Investigations are being conducted of the role of water – water converts oxide to hydroxide, which can then exchange isotope labels. If the oxygen control technique allows either water or

hydrogen to accumulate, then a less resistant oxide and isotope exchange may be expected. This hypothesis will be tested using ^{18}O labeled 316 and D9, using the OCS and thermal decomposition of metal oxides (the methodology of the gas phase experiments) to set oxygen/water/hydrogen levels. Iron and chromium isotope labels can be used at a later stage of investigations to determine metal ion mobility.

Collaborative work continued; samples have been supplied by UNLV for investigation using nano-indentation, AFM, and more recently TEM and XRD by collaborators. These have shown new structures in the protective oxide, and will be used to continue the development of the fundamental corrosion model. Also, analytical results have been provided to collaborators for samples prepared elsewhere, (e.g. LANL).

Impact of Silicon on Corrosion Resistance of Stainless Steels in LBE Systems (Task 20).

Research work performed during this quarter was focused on the evaluation of the effect of activation on the tensile properties of T91 grade steels with different silicon content at ambient temperature. In addition, substantial efforts were focused on the determination of the cracking susceptibility of all four experimental heats of T91 grade steels in the presence of a 100 C acidic solution using double-cantilever-beam (DCB), C-ring, and U-bend specimens. The corrosion rates of these alloys were also determined based on the weight-loss in a similar environment. Further, the tensile properties of martensitic steels containing greater than 2 wt% Si were evaluated at ambient and elevated temperatures.

The results of tensile testing involving activated smooth cylindrical specimens of all four heats are shown in Figures 37-40 in the form of superimposed engineering stress versus strain (s-e) diagrams. They also illustrate s-e diagrams for specimens with no activation. An evaluation of these diagrams clearly reveals higher strength but reduced ductility, indicating radiation-hardening due to the application of electron beams. The extent of hardening was more pronounced at longer activation times, as anticipated. The tensile strength at comparable activation times was at a minimum for the steel containing 2 wt% Si.

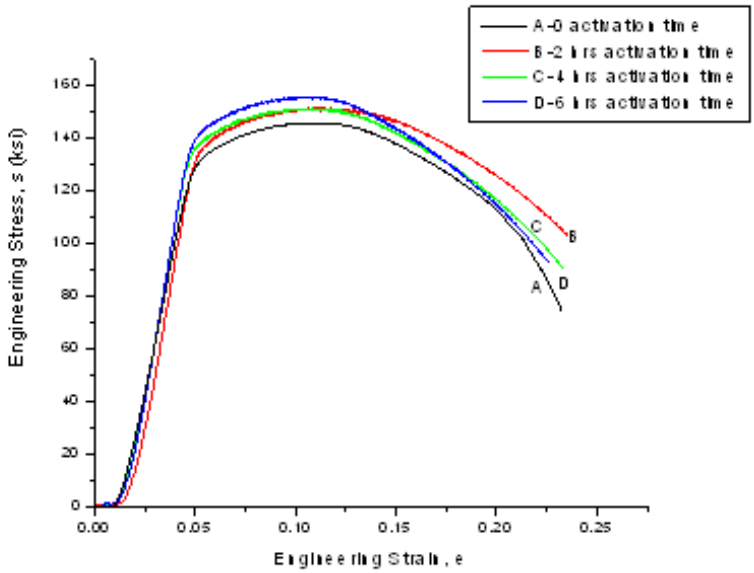

Figure 37: Comparison of s-e Diagrams for Steel Containing 0.5 wt% Si.

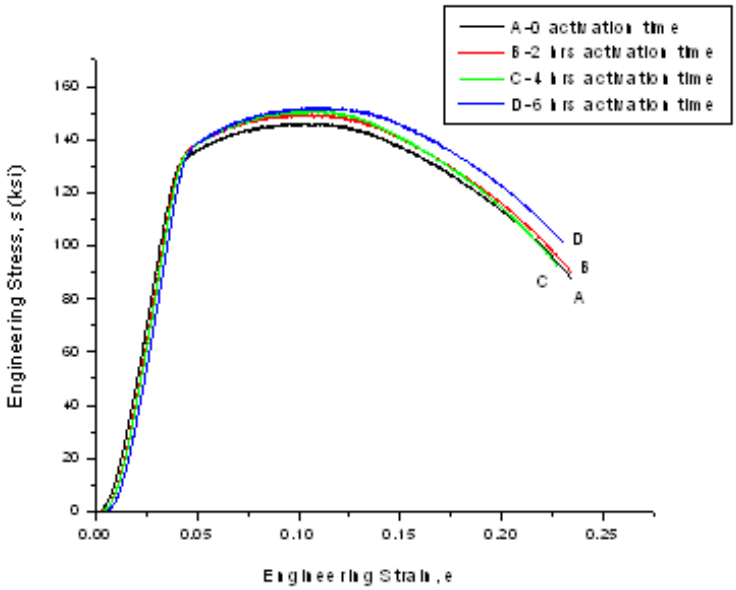

Figure 38: Comparison of s-e Diagrams for Steel Containing 1.0 wt% Si.

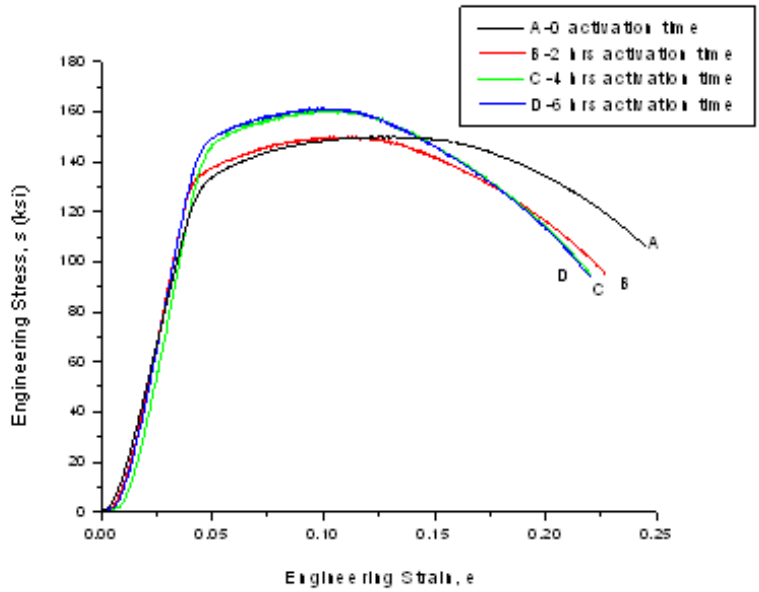

Figure 39: Comparison of s-e Diagrams for Steel Containing 1.5 wt% Si.

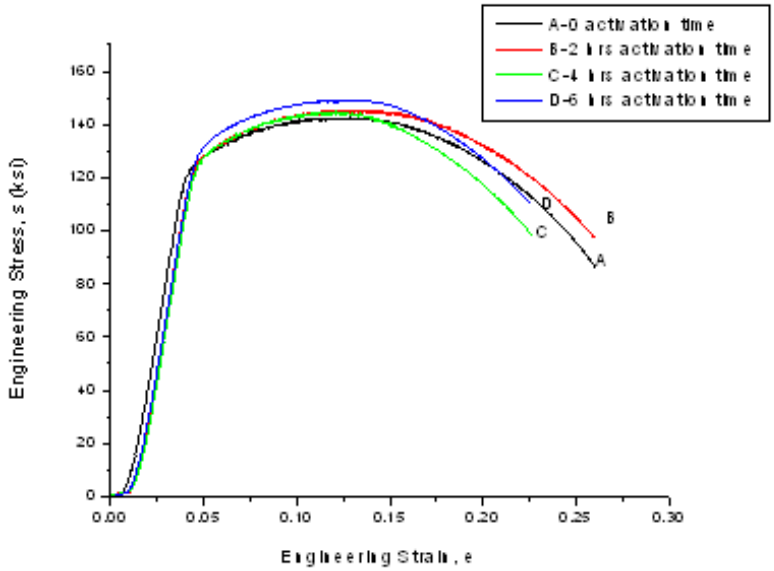

Figure 40: Comparison of s-e Diagrams for Steel Containing 2.0 wt% Si.

The magnitudes of both the initial stress intensity factor (K_i) and the final stress intensity factor (K_f), obtained from DCB testing, are given in Table 6. These data indicate that the magnitude of the final load was reduced in all tested specimens, the reduction being more pronounced with specimens loaded to higher K_i values. For the same reason, the difference in stress intensity factor (ΔK), before and after testing, also increased with higher K_i values. A maximum ΔK value was seen with the DCB specimens of T91 grade steel with 2 wt% Si. A metallographic montage of a broken DCB specimen made of steel with 2 wt % Si is illustrated in Figure 41, showing different types of cracking.

Table 6: Results of DCB Testing

Heat No. / Si Content	Initial Wedge Load (lbf)	Final Wedge Load (lbf)	a_i (in)	a_f (in)	Δa (in)	K_i (ksi$\sqrt{in}$)	K_f (ksi$\sqrt{in}$)	ΔK (ksi$\sqrt{in}$)	Test Duration (days)	CGR (in/hour)
2403 / 0.5 wt% Si	600	485	1.329	1.644	0.315	35.21	33.82	1.39	60	21.9×10^{-5}
	900	700	1.329	1.683	0.354	52.81	49.78	3.03	30	49.2×10^{-5}
2404 / 1.0 wt% Si	800	680	1.329	1.565	0.236	46.94	45.54	1.40	60	16.4×10^{-5}
	1200	980	1.329	1.604	0.275	70.41	66.98	3.43	60	19.1×10^{-5}
2405 / 1.5 wt% Si	1000	850	1.329	1.565	0.236	58.68	56.92	1.75	60	16.4×10^{-5}
	1400	1050	1.329	1.762	0.373	82.15	78.68	3.47	30	51.8×10^{-5}
2406 / 2.0 wt% Si	800	650	1.329	1.565	0.236	46.94	43.01	3.94	30	32.8×10^{-5}
	1200	900	1.329	1.644	0.315	70.41	62.76	7.66	60	21.9×10^{-5}

a_i = Initial crack length
a_f = Final crack length
Δa = Change in crack length
ΔK = Change in stress intensity factor
CGR = Overall crack growth rate

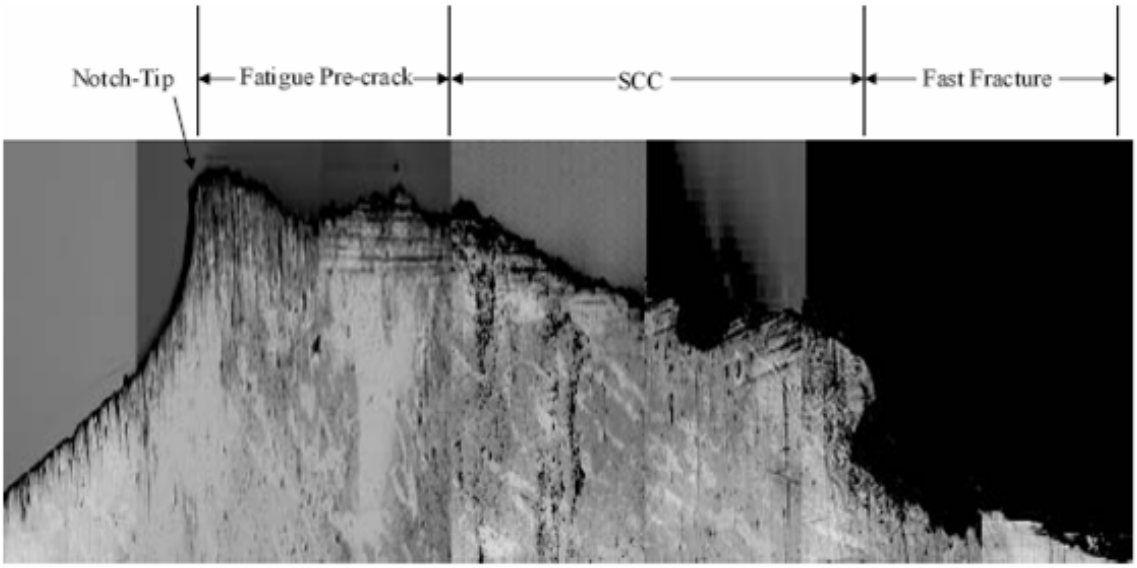

Figure 41: Metallographic Montage of a Broken DCB Specimen (2.0 wt% Si), Beraha's Reagent, 20x.

An evaluation of the C-ring and U-bend specimens by SEM revealed intergranular cracking on the convex surfaces of a few specimens. The maximum stress was experienced on the convex surface due to the tensile loading.

The results of immersion testing involving coupons of all four heats of T91 grade steel in a 100 C acidic solution is given Table 7. These results indicate that there was a gradual drop in

corrosion rate in terms of mpy with increased Si content up to 1.5 wt%. A relatively higher corrosion rate was, however, observed with steel containing 2 wt% Si.

Table 7: Results of coupon testing.

Heat No. / Si Content	W_i (gms)	W_f (gms)	W (mg)	Corrosion Rate (mpy)
2403/ 0.5 wt% Si	7.072	6.978	94	6.571
2404/ 1.0 wt% Si	7.137	7.055	82	5.732
2405/ 1.5 wt% Si	7.019	6.993	26	1.817
2406/ 2.0 wt% Si	7.037	6.969	68	4.753

W_i = Initial Weight W_f = Final Weight W = Weight-Loss mpy = Mils per Year

The tensile data involving smooth cylindrical specimens of martensitic steels containing higher Si content (2.75, 4.83 and 5.27 wt%) are illustrated in Figures 42-44 in the form of superimposed s-e diagrams at different temperatures. These results indicate that at higher Si content (4.83 and 5.27 wt%), significant brittleness was observed, showing no plastic deformation at ambient temperature. The lack of plastic deformation at ambient temperature is the result of brittleness associated with the presence of high Si content. However, plastic deformation was observed at elevated temperatures, showing better ductility, as expected.

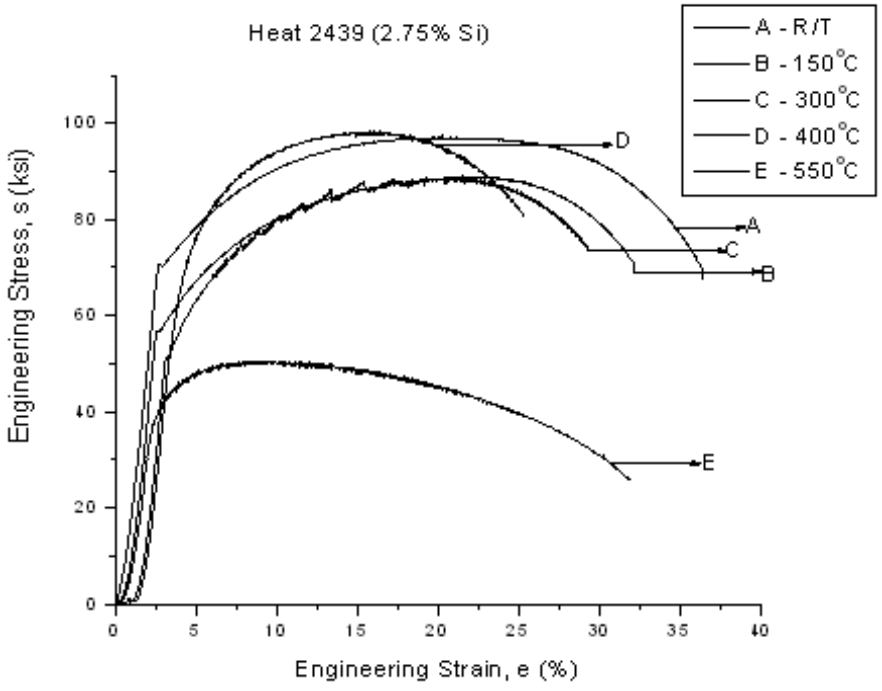

Figure 42: Comparison of s-e Diagrams for Steel Containing 2.75 wt% Si.

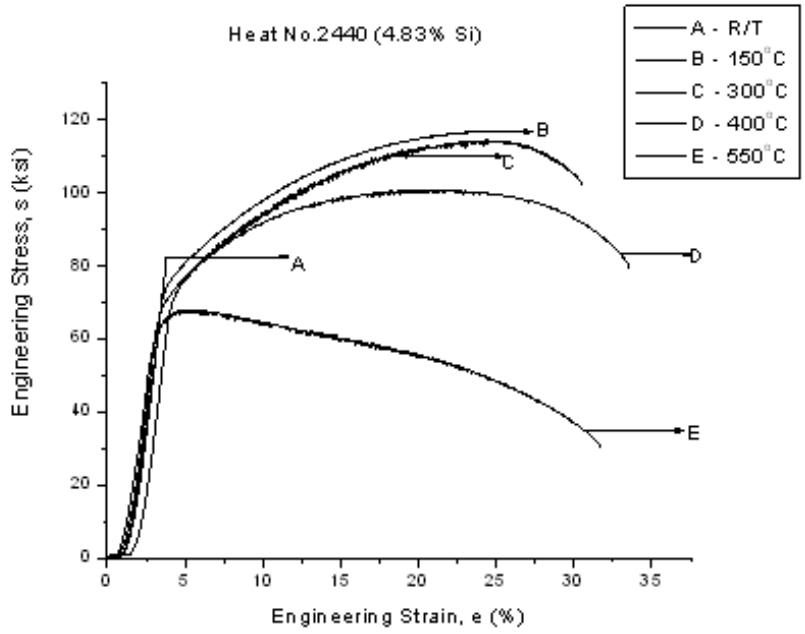

Figure 43: Comparison of s-e Diagrams for Steel Containing 4.83 wt% Si.

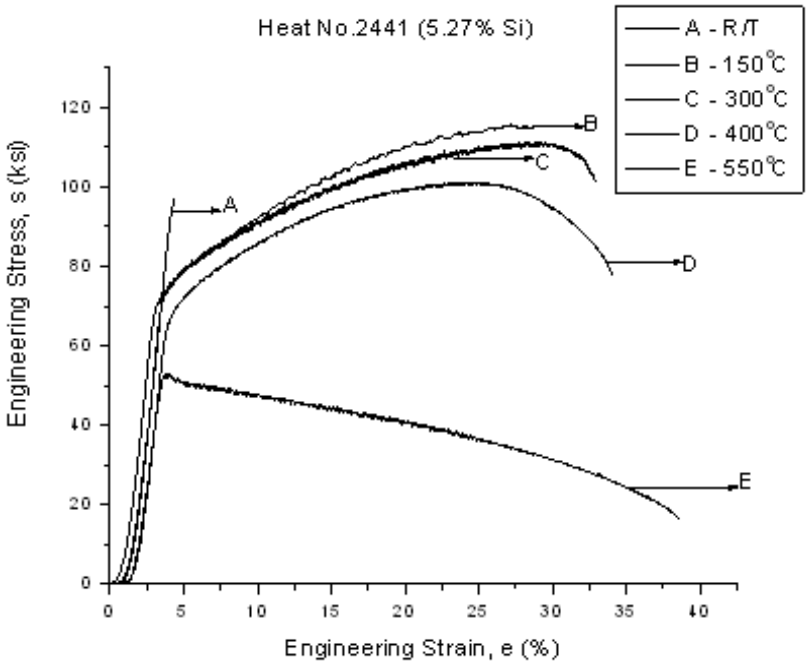

Figure 44: Comparison of s-e Diagrams for Steel Containing 5.27 wt% Si.

Oxide Film Growth Modeling in LBE Systems (Task 21).

Parametric study on the oxidation process coupled with inward oxygen diffusion using a cellular automaton method

A cellular automaton (CA) model for the oxidation process, coupled with inward oxygen diffusion, was developed. A parametric study was conducted to check the control variable on the oxidation behavior for at long times. The simulation results under different control variables are shown Figures 45-48. Both of the effects of K_d (mass transport ratio between oxygen and iron walker) and P_{act} (the reaction probability) on oxide growth have been investigated. The oxygen concentration in the liquid LBE is taken as 0.2. The snap shot for the mesoscopic oxide structure's 200,000th time step is shown in Figure 45. Comparing the thickness of the oxide layer, it can be found that the larger reaction probability results in thicker oxide layer. The oxide thickness as a function of time step under different P_{act} is shown Figure 46. As indicated in the figures, it can be found that the increasing of P_{act} from a small value for a given time step will increase the oxide thickness and then the oxide layer almost keeps the same growth rate after P_{act} reaches the critical value. The reason for this phenomenon can be understood once one realizes that the iron walker which is formed by the reaction will be saturated when P_{act} exceeds one critical value. Figures 47 and 48 show the walker and oxygen distribution for different P_{act}.

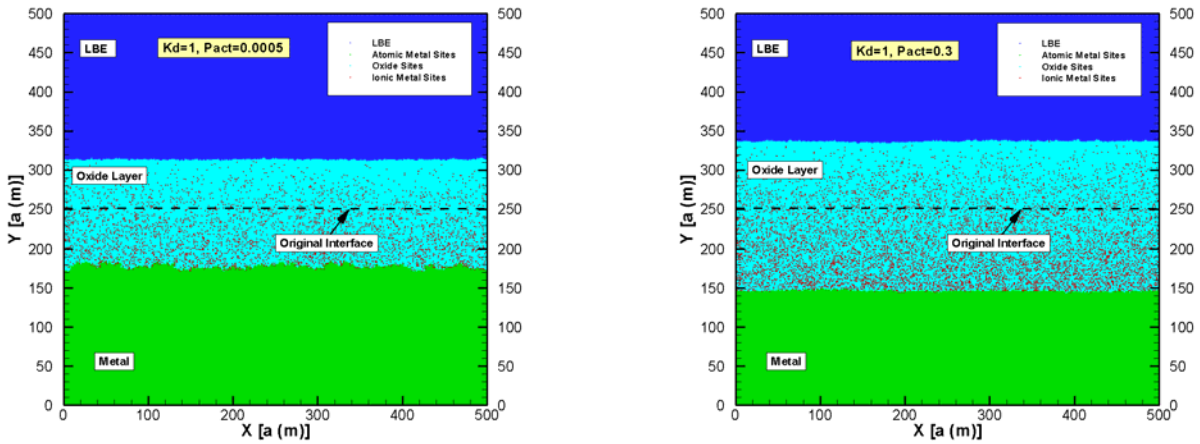

(a) P_{act} = 0.0005 *(b) P_{act} = 0.3*

Figure 45: The snapshot of the mesoscopic oxide structure at N_t = 200,000. Here, K_d = 1 and C_0 = 0.2.

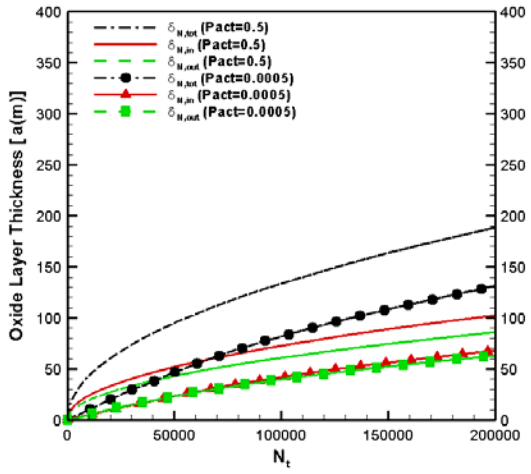

(a) P_{act} = 0.0005

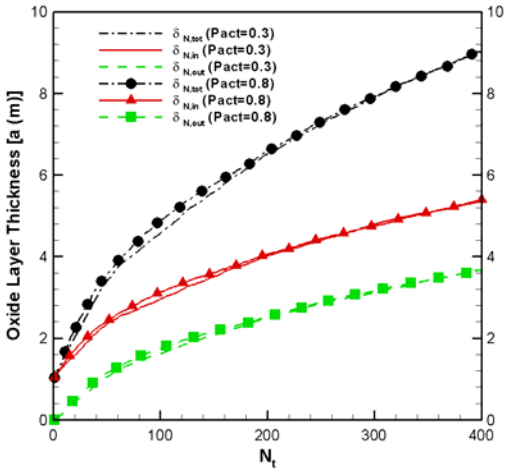

(b) P_{act} = 0.3

Figure 46: The comparison of the oxide layer thickness of cases at different P_{act}. Here, K_d = 1 and C_0 = 0.2.

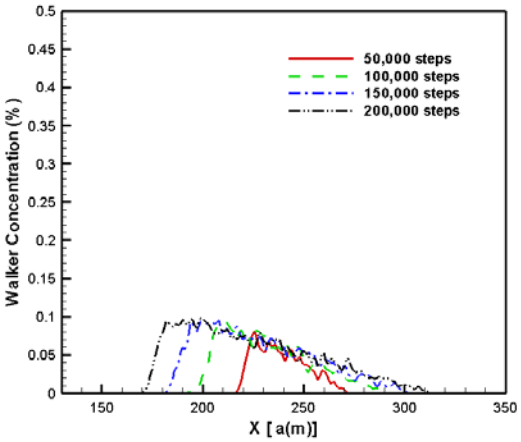

(a) P_{act} = 0.0005

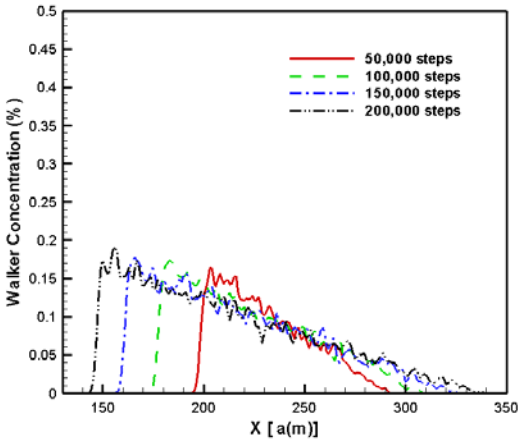

(b) P_{act} = 0.3

Figure 47: The walker distributions for N_t = 200,000 at different P_{act}. Here, K_d = 1 and C_0 = 0.2.

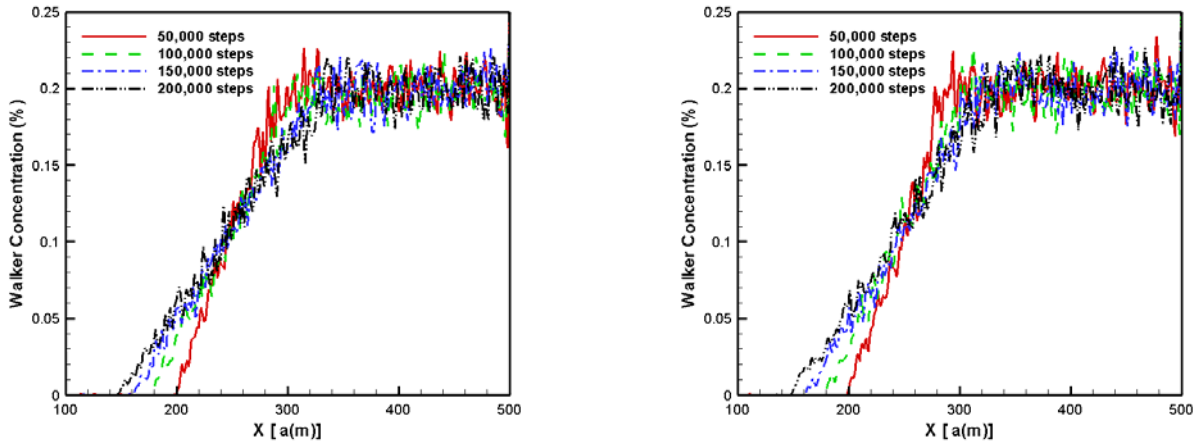

(a) P_{act} = 0.0005 *(b) P_{act} = 0.3*

Figure 48: The oxygen distributions for N_t = 200,000 at different P_{act}. Here, K_d = 1 and C_0 = 0.2.

Reactor Physics Studies for the AFCI RACE Project (Reactor-Accelerator Coupling Experiments Project (Task 27).

Analysis continued of ISU RACE experiments conducted last October with the Monte Carlo code MCNPX. A computational approach based on power iterations method (KCODE) to directly assess the efficiency of delayed neutrons is under development. The shape function for the steady-state problem, which is used as a weighting function, was calculated and the relative efficiency of neutrons causing fission was determined. The effective fraction of delayed neutrons (β_{eff}) was assessed (Figure 49) for the ISU RACE subcritical assembly based on the calculation of the relative efficiency of fission induction from delayed versus prompt neutrons. The average calculated efficiency was 1.123. Combining this result with a steady-state mode, the equivalent beta-effective (delayed neutron fraction) is 0.771%.

Evaluation continued of experimental thermal and neutron generation with the UNLV High-power RACE target (experiments were conducted at ISU). Modeling continued of the target using Gambit and the CFD code FLUENT for comparison with experiments. Refinement of the MCNPX transport model continued to reduce statistical uncertainty. Parametric studies are being performed to study impacts of accelerator performance and characteristics, such as beam spread in energy or position.

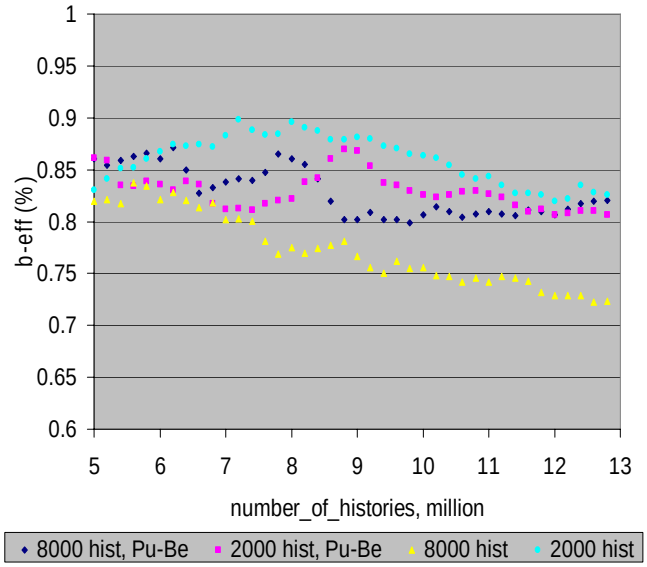

Figure 49: Calculated Effective Delayed-Neutron Fraction (β_{eff}) versus number of MCXNP histories.

Decoupling and Disturbance Rejection Control for Target Circulation (Task 31).

The whole TC-1 system was tested and continuously operated for 20 days. All of the operation components (target, heat exchanger, EM pump, drainage tank, compensation tank, siphon device, etc) are in one compact container, making thermal control complicated. In addition, the safety issue has to be taken into account since this system is at UNLV, and will be operated by students with little experience. Furthermore, operation procedures are not simple. After the alarm system, monitoring system, and dial-out system were successfully tested, the TC-1 system was continuously run for several types of testing,

TC-1 was heated up to 200 C and maintained at the working range of 190 to 200 C. The control of TC-1 satisfied all the technical requirements as shown in Figure 50: the heating rate was not to exceed 50 C/hour, the temperature difference between all heating zones (excluding Zones 1 and 2) are less than 20 C, at the heating period (including melting process), Zone 1 must be 50 C higher than Zone 2, the temperatures of all heating zones are in the setting range while maintaining the process.

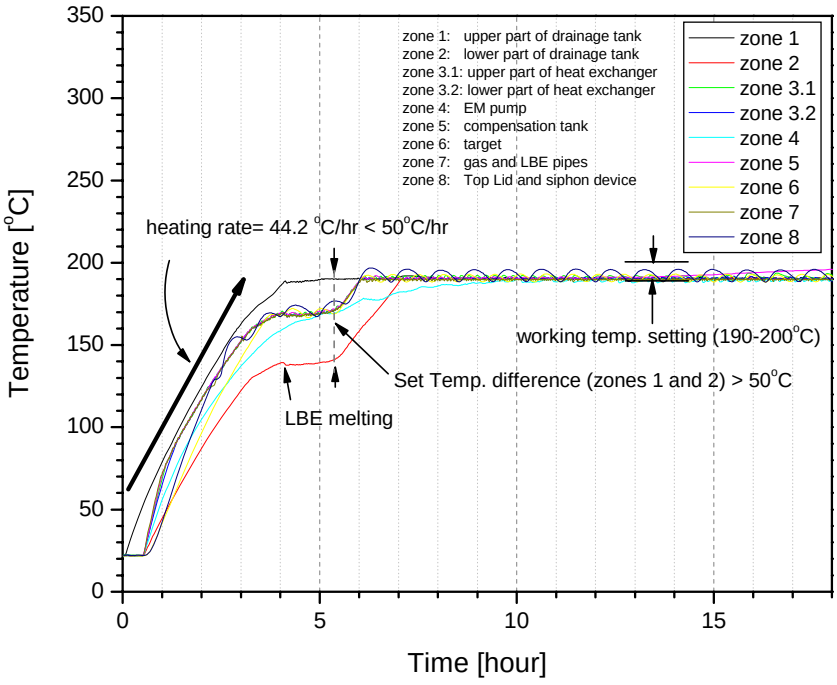

Figure 50: The heating and maintaining processes of TC-1.

The filling and draining processes were tested. Level meter indicators were installed on the panel of the gas control system for user-friendly operation. The EM pump was tested. Thermal disturbances of EM pump to other heating zones, including its own, were obtained. The EM flow meter was tested. The cooling control process of TC-1 was tested. The 24-hour alarm system was tested and worked properly for more than 25 days.

The following problems were found and resolutions are provided:

- One valve from the siphon device on the top of TC-1 was leaking when checked. Operation procedures were modified to bypass this problem.
- One of the current measurement transducers was corrected to obtain the actual reading.
- It is impossible to control the temperature by only using heaters in each heating zone to maintain a certain working temperature range if the EM pump is ON (Figure 51). An external cooling process has to be used.
- Zero drift of the flow meter reading was solved.
- It took more than 18 days to cool the TC-1 from high temperature to room temperature. The well-insulated material prohibits the natural cooling process. The highest temperature zone is the compensation tank (Figure 52).

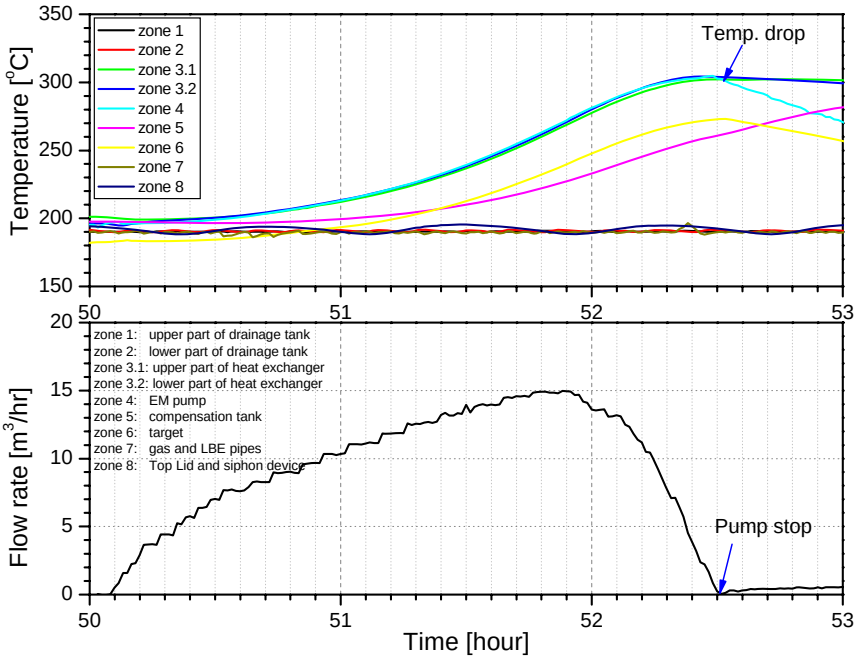

Figure 51: The responses of all heating zones under condition of EM pump ON.

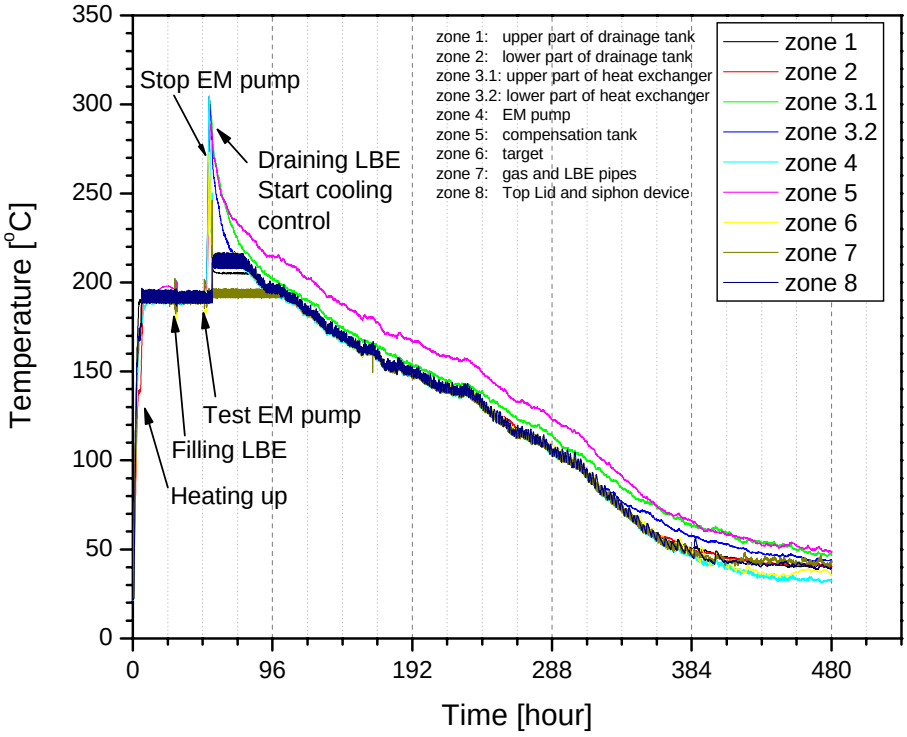

Figure 52: The temperature profiles of 8 heating zones under heating, maintain, LBE filling, pump-on, LBE draining, and cooling conditions.

The following are some options for improved performance:

- The slow cooling process can be sped up using one blower or cool air pipe at the position where the compensation tank is located (Figure 53).
- Better efficiency of the EM pump can be achieved using a variable frequency driver to reduce the extra heat generated by EM pump.
- The heat generated by the EM pump can be removed by an air-conditioning system, avoiding an expensive investment for a secondary cooling circulation using a heat exchanger in the TC-1. Forced cool air passing through the pipe sections (heat radiation) of the by-pass system will achieve this purpose.
- The cooling water circulation in the radiation shield loop would be tested to get the additional heater in the well insulated enclosure.
- Forced air flow into heater exchanger component in TC-1 should be studied.

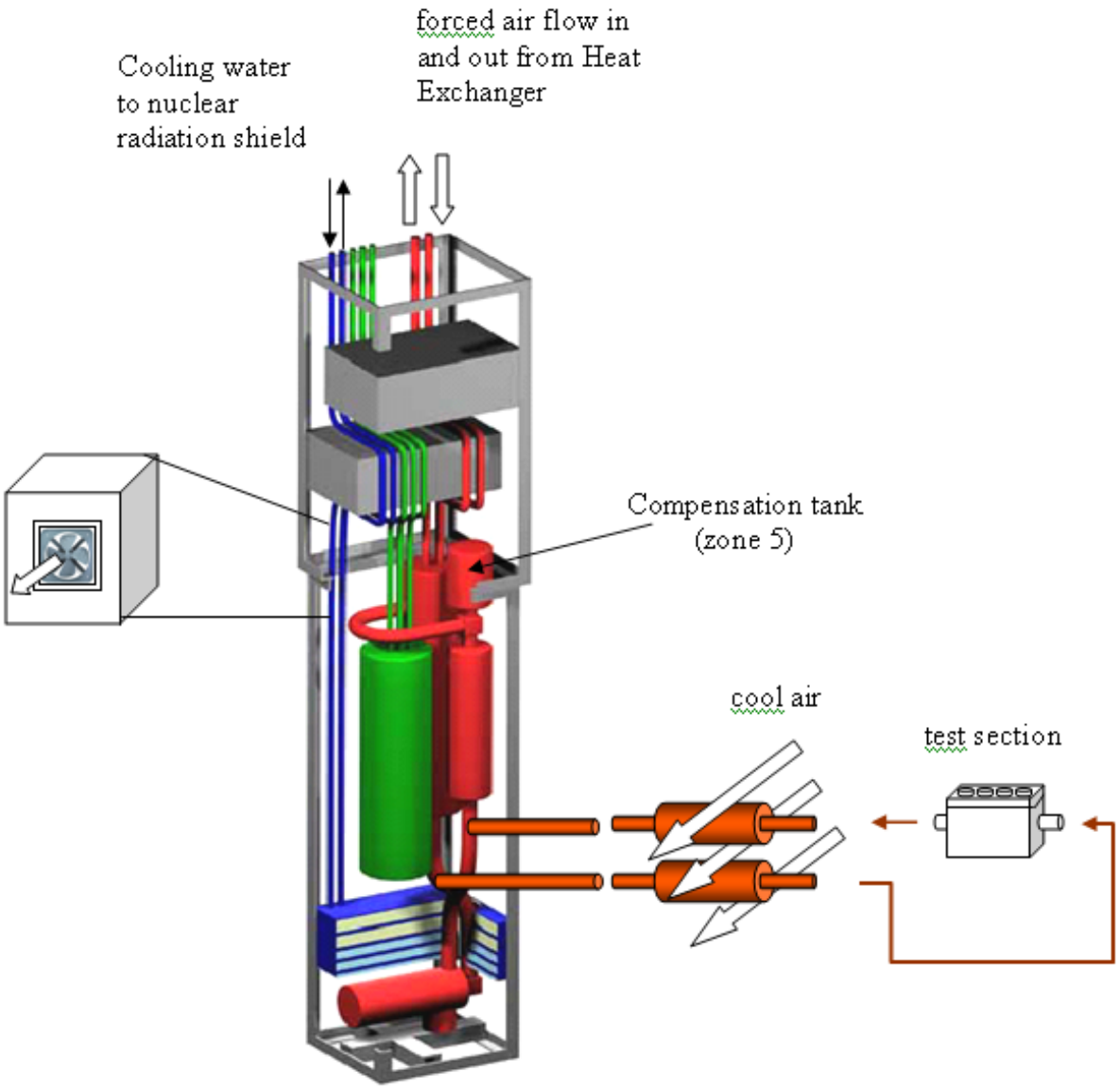

Figure 53. TC-1 schematic diagram with options for cooling.

Magnetohydrodynamic Simulation of Electromagnetic Pump in TC-1 (Task 32).

Online database activity

An on-line literature database has previously been set up at:
http://nstg.nevada.edu/mmrg/research/LitSurvey/EMP-Literature.html
and now contains over 120 entries. One of the issues that arose during development was that only a single user had access to enter new articles into the database. This meant that quite often, valuable articles were not being made available to all users. It was decided to develop a wiki-based database to allow all members of the research group to enter and edit database entries. According to Wikipedia (the most well-know wiki), a wiki is "a collaborative website which can be directly edited by anyone with access to it." One of the advantages of wikis is that they allow

easy exchange of information between individuals working on a single project. The wiki for this project is currently in the beta-testing stage and will be fully functional by the end of August 2007.

EMPUMPER development

The results of a numerical model of the TC-1 loop calculated only the EM phenomena (current density, magnetic field, and electromagnetic body forces) in the pump. The velocity of the liquid was specified, not calculated. In addition, the EM phenomena were calculated using analytic expressions that were based on geometrical simplifications. The next generation of the model, which has been under development (EMPUMPER), will calculate both the EM as well as the fluid flow phenomena and will thus be a fully coupled MHD solver. The CFD portion of the code has been completed and tested against analytic test cases and a similar model developed using StarCD.

Criticality Studies for UREX Processes (Task 35).

The project scope continued to be defined, and the appropriate focus on cross-section sensitivity studies versus design of required criticality experiments was examined. Students continued to collect information on code systems and references on criticality and sensitivity studies and to research cross section uncertainties for Am and Cm at room temperature in UREX+1 separations processes. Previously, MCPX, MCNPX, SCALE, and data libraries for processing cross sections and conducting sensitivity studies were acquired and installed. This quarter NJOY 99 was acquired and installed for processing cross sections for sensitivity studies. In addition, sample problems for Scale 5.1 were completed to ensure accuracy of the code.